The Astronomical Journal, 140:1787–1805, 2010 December doi:10.1088/0004-6256/140/6/1787

MIXED-MORPHOLOGY SUPERNOVA REMNANTS IN X-RAYS: ISOTHERMAL PLASMA IN HB21 AND PROBABLE OXYGEN-RICH EJECTA IN CTB 1

Thomas G. Pannuti[1,4,5], Jeonghee Rho[1,6], Kazimierz J. Borkowski[2], and P. Brian Cameron[3]
[1] Spitzer Science Center, California Institute of Technology, MS 220-6, Pasadena, CA 91125, USA
[2] Department of Physics, North Carolina State University, Box 8202, Raleigh, NC, 27695, USA; kborkow@unity.ncsu.edu
[3] Division of Physics, Mathematics and Astronomy, 105-24, California Institute of Technology, Pasadena, CA 91125, USA; pbc@astro.caltech.edu
Received 2006 February 2; accepted 2010 September 15; published 2010 November 3

ABSTRACT

We present an analysis of X-ray observations of the Galactic supernova remnants (SNRs) HB21 (G89.0+4.7) and CTB 1 (G116.9+0.2), two well-known members of the class of mixed-morphology (MM) SNRs. Our analysis draws upon observations of both SNRs made with the *Advanced Satellite for Cosmology and Astrophysics* (*ASCA*): we have also used an archived *Chandra* observation of CTB 1 as part of this effort. We find a marked contrast between the X-ray properties of HB21 and CTB 1: in the case of HB21, the extracted spectra of the northwest and southeast regions of the X-ray-emitting plasma associated with the SNR can be fit with a single thermal model with marginally enhanced silicon and sulfur abundances. For both of these regions, the derived column density and temperature are $N_{\rm H} \sim 0.3 \times 10^{22}$ cm^{-2} and $kT \sim 0.7$ keV, respectively. No significant spatial differences in temperature or elemental abundances between the two regions are detected and the X-ray-emitting plasma for both regions is close to ionization equilibrium. Our *Chandra* spectral analysis of CTB 1 reveals that this source is likely an oxygen-rich SNR with enhanced abundances of oxygen and neon: this result is quite surprising for an evolved SNR like CTB 1. The high angular resolution *Chandra* observation of CTB 1 reveals spectral variations across this SNR: in particular, we have detected localized hard emission with an angular extent of $\sim 1'$. The extracted *ASCA* spectra for both the southwest and northeastern regions of CTB 1 cannot be fit with a single thermal component and instead an additional component is required to account for the presence of excess emission seen at higher energies. Based on our fits to the extracted *ASCA* spectra, we derive a column density $N_{\rm H} \sim 0.6 \times 10^{22}$ cm^{-2} and a temperature for the soft thermal component of $kT_{\rm soft} \sim 0.28$ keV for both regions. The hard emission from the southwest region may be modeled with either a thermal component with a temperature $kT_{\rm hard} \sim 3$ keV or by a power-law component with a photon index $\Gamma \sim 2$–3; for the northeast region, the hard emission may be modeled with a power-law component with a photon index $\Gamma = 1.4$. The detection of center-filled ejecta-dominated X-ray emission from HB21 and CTB 1 as well as other MM SNRs suggests a new scenario for the origin of the contrasting X-ray and radio morphologies of this class of sources. Lastly, we have analyzed the properties of the discrete hard X-ray source 1WGA J0001.4+6229 which is seen in projection just inside the northeastern shell of CTB 1. Our extracted *ASCA* GIS spectra of this source are best fit using a power-law model with a photon index $\Gamma = 2.2^{+0.5}_{-1.2}$: this slope is typical for featureless power-law continua produced by rotation-powered pulsars. This source may be a neutron star associated with CTB 1. We find marginal evidence for X-ray pulsations from this source with a period of 47.6154 ms. A deep radio observation of this source failed to reveal any pulsations.

Key words: ISM: individual objects (SNR 089.0+04.7, SNR 116.9+00.2, 1WGA J0001.4+6229) – ISM: supernova remnants – X-rays: ISM

Online-only material: color figures

1. INTRODUCTION

A new morphological class of supernova remnants (SNRs) known as the mixed-morphology (MM) SNRs has been firmly established in the recent literature (Rho & Petre 1998; Shelton et al. 1999). The defining characteristics of SNRs of this class include a shell-like radio morphology combined with a centrally filled X-ray morphology. X-ray observations of these SNRs made with *ROSAT*, the *Advanced Satellite for Cosmology and Astrophysics* (*ASCA*), *Chandra*, and *XMM-Newton* have found that the central X-ray emission from these SNRs is not non-thermal emission (as would be expected from a central plerion) but instead thermal emission from shock-heated swept-up interstellar material. Examples of well-known MM SNRs include W28 (Rho & Borkowski 2002), G290.1−0.8 (MSH 11−61*A*) (Slane et al. 2002), and IC 443 (Kawasaki et al. 2002). Rho & Petre (1998) suggested that as many as 25% of the entire population of Galactic SNRs may belong to this morphological class. Based on CO and infrared observations (Koo et al. 2001; Reach et al. 2005), it appears that many MM SNRs are interacting with nearby molecular and H I clouds. This result suggests a connection between the contrasting X-ray and radio morphologies of these SNRs with the interaction between these sources and adjacent clouds, but such a connection lacks a detailed theoretical basis at this time. Two leading scenarios have been advanced to explain the origin of the contrasting radio and X-ray morphologies of MM SNRs: in the first scenario—known as the evaporating clouds scenario—molecular clouds overrun by the expanding shock front of the SNR survive passage through the shock and eventually evaporate, providing a source

[4] Guest User, Canadian Astronomy Data Center, which is operated by the Dominion Astrophysical Observatory for the National Research Council of Canada's Herzberg Institute for Astrophysics.
[5] Currently at Space Science Center, Department of Earth and Space Sciences, 235 Martindale Drive, Room 212E, Morehead State University, Morehead, KY 40351, USA; t.pannuti@moreheadstate.edu
[6] Currently at SOFIA Science and Mission Operations/USRA, NASA Ames Research Center, MS 211-3, Moffett Field, CA 94035, USA; jrho@sofia.usra.edu

of material that increases the density of the interior X-ray-emitting plasma of the SNR (Cowie & McKee 1977; White & Long 1991). In the second scenario—known as the radiative shell model—the SNR has evolved to an advanced stage where the shock temperature is low and very soft X-ray emission from the shell is absorbed by the interstellar medium (ISM): therefore, the only detectable X-ray emission is from the interior of the SNR (Cox et al. 1999; Shelton et al. 1999, 2004). In the current paper, we analyze and discuss X-ray emission from two Galactic SNRs—HB21 and CTB 1—which have both been previously classified as MM SNRs by Rho & Petre (1998).

HB21 (G89.0+4.7) was discovered in a radio survey by Brown & Hazard (1953). The radio angular extent of this SNR is large—120 × 90 arcmin (Green 2009a)—and the radio morphology is a closed shell. The shell appears to be flattened along the eastern boundary and features bright regions along the northern and southern boundaries with a prominent indentation seen along the northern boundary. The radio emission from HB21 is strongly polarized (3.7% ± 0.4%) with a projected magnetic field tangential to the shell (Kundu 1971; Kundu et al. 1973; Kothes et al. 2006), suggesting that the shell was compressed during the radiative evolutionary stage of the SNR. The measured radio spectral index for this SNR is $\alpha \sim 0.4$ ($S_\nu \propto \nu^{-\alpha}$) (Leahy 2006; Green 2009b) but significant variations in the values (from 0.0 to 0.8 with a standard deviation of 0.16) of the spectral index across the face of the SNR were observed by Leahy (2006). Based on *IRAS* observations, Saken et al. (1992) detected clumpy infrared filaments associated with this SNR. Filamentary optical emission from this SNR with an angular extent comparable to the radio shell was detected by Mavromatakis et al. (2007). Extensive evidence exists that indicates HB21 is interacting with adjacent molecular clouds: this evidence includes CO observations (Tatematsu et al. 1990; Koo et al. 2001; Byun et al. 2006) as well as near- and mid-infrared observations of the sites of shock-molecular cloud interactions along the northern and southern parts of the SNR (Shinn et al. 2009, 2010). H I observations toward HB21 (Tatematsu et al. 1990; Koo & Heiles 1991) have revealed a high velocity expanding shell associated with this SNR. Finally, HB21 has been the subject of prior pointed X-ray observations made by Einstein (Leahy 1987) and *ROSAT* (Rho 1995; Leahy & Aschenbach 1996)): in this paper we include the *ROSAT* images presented previously by Rho (1995) in her PhD thesis work. No pulsars or γ-ray sources are believed to be associated with HB21: radio searches for a pulsar associated with this SNR were conducted by Biggs & Lyne (1996) and Lorimer et al. (1998), but no candidate sources were found. The distance to HB21 is not well known: Tatematsu et al. (1990) argued for a distance of only 0.8 kpc based on an association between the SNR and molecular material that belongs to the Cygnus OB7 association (Humphreys 1978). However, Yoshita et al. (2001) suggested a distance of $\geqslant$1.6 kpc based on a correlation that those authors found between X-ray absorbing column density and extinction, and Byun et al. (2006) suggested a distance of 1.7 kpc based on CO observations. In this paper, we have adopted a distance of 1.7 kpc to HB21.

CTB 1 (G116.9+0.2) was discovered in a survey of Galactic radio emission at 960 MHz by Wilson & Bolton (1960). Subsequent radio observations of this SNR (Velusamy & Kundu 1974; Angerhofer et al. 1977; Landecker et al. 1982; Yar-Uyaniker et al. 2004; Tian & Leahy 2006; Kothes et al. 2006) reveal a radio morphology that may be described as a nearly complete circular shell with a diameter of approximately 34 arcmin (Green 2009b). The radio emission is brightest along the western rim and a prominent gap is seen along the northern and northeastern sectors of the circular emission. Like HB21, the magnetic field is aligned in the tangential direction, also suggesting that the shell was compressed during the radiative stage of the evolution of the SNR, but compared to HB21 the degree of polarization is much lower (0.4% ± 0.1%—see Kothes et al. 2006). The measured spectral index of the observed radio emission is $\alpha \sim 0.6$ (Landecker et al. 1982; Kothes et al. 2006; Tian & Leahy 2006; Green 2009b). CTB 1 has also been detected at optical wavelengths, in emission lines such as [O III] λ5007 and [S II] λλ 6716, 6731; the observed optical shell-like morphology closely matches the radio shell. The optical images of CTB 1 presented by Fesen et al. (1997) depict a remarkable contrast in the emission-line properties of this SNR: while [S II] emission is seen from roughly the entire optical shell (with the greatest amount of emission in the south), the [O III] emission appears to be almost entirely localized to the western rim of the shell. Saken et al. (1992) detected infrared emission from CTB 1 in the 60 μm and 100 μm *IRAS* bands: an arc of infrared emission was seen in the 60 μm/100 μm ratio image that appears to be coincident with the radio shell. CTB 1 was observed in X-rays with *ROSAT* (Hailey & Craig 1995; Rho 1995; Craig et al. 1997): like other MM SNRs, the X-ray emission from this SNR (which has a thermal origin) lies interior to the radio and optical shells. Remarkably, the X-ray emission is also seen to extend through the known northern gap of the SNR. Like HB21, no pulsars or γ-ray sources are believed to be associated with CTB 1: a radio search conducted by Lorimer et al. (1998) for a pulsar revealed no candidate sources. Published distance estimates for this SNR have ranged from 1.6 to 3.5 kpc; in this paper, we have adopted a distance to CTB 1 of 3.1 ± 0.4 kpc as measured by Hailey & Craig (1994).

The organization of this paper is as follows. In Section 2, we describe the *ASCA* X-ray observations of HB21 and CTB 1 and the *Chandra* observations of CTB 1, including details of data reduction. *ROSAT* and radio observations of these SNRs are also described in this section. In Section 3, we present the results of our spectral analyses for both HB21 and CTB 1 (in Sections 3.1 and 3.2, respectively). In Section 4, we discuss the nature of the hard discrete X-ray source 1WGA J0001.4+6229: we have discovered weak evidence for pulsed X-ray emission from this source (which is seen in projection against CTB 1) and consider the possibility that it is a neutron star associated with CTB 1. We also present a search for radio pulsations from 1WGA J0001.4+6229. Interpretations of our X-ray results for HB21 and CTB 1 are presented in Sections 5 and 6, respectively. We also detected hard X-ray emission from CTB 1: we discuss the nature of this emission in Section 7. Our preliminary results of this paper have been presented in Pannuti & Rho (2004) after which we note that similar data sets were analyzed and presented by Lazendic & Slane (2006). Our primary results of HB21 are in agreement with and strengthen those of Lazendic & Slane (2006); for CTB 1, our paper presents extensive and thorough analysis of the *Chandra* and *ASCA* data in smaller-scale regions. We also report important new results for this SNR, including the probable detection of oxygen-rich ejecta from CTB 1 as well as spectral variations across the object. In addition, an X-ray hard point-like source is identified and an analysis of its X-ray and radio properties is presented. Finally, the conclusions of this work are summarized in Section 8.

2. OBSERVATIONS AND DATA REDUCTION

2.1. ASCA Observations of HB21 and CTB 1

Because the X-ray emission from both HB21 and CTB 1 cover a large angular extent on the sky, two pointed observations were made of each SNR with *ASCA* (Tanaka et al. 1994), namely, the southeast and northwest regions of HB21 and the southwest and northeast regions of CTB 1 (see Table 1 for details of these observations). These observations provided almost a complete spatial coverage of the X-ray-emitting gas in both SNRs. The data reduction was conducted using the "XSELECT" program (Version 2.2), which is available from the High Energy Astrophysics Science Archive Research Center (HEASARC[7]). There were two types of instruments on board *ASCA*—the Gas Imaging Spectrometer (GIS) and the Solid-State Imaging Spectrometer (SIS)—and both of these instruments were composed of two units denoted as GIS2, GIS3, SIS0, and SIS1, respectively. A single GIS unit sampled a field of view $\sim 50'$ in diameter and a background count rate of the GIS is 5×10^{-4} counts cm^{-2} s^{-1} keV^{-1}; in comparison, a single SIS unit sampled a field of view approximately $44' \times 44'$ in size. The nominal FWHM angular resolution of both the GIS and SIS units was approximately 1 arcmin. The standard REV2 screening criteria were applied when reducing both the raw GIS and SIS data sets. We used "FMOSAIC" from the FTOOLS software package to generate an X-ray map by combining the GIS2 and GIS3 maps. We used the FTOOL "MKGISBGD" to prepare blank-sky background spectra and images for each extracted GIS source spectra: for these background data sets, point sources which are brighter than approximately 10^{-13} erg cm^{-2} s^{-1} have been removed. Similarly, background spectra were generated using standard SIS blank-sky data sets for analyzing the extracted SIS source spectra. The standard GIS2 and GIS3 response matrix files (RMFs) were used for analyzing extracted the GIS source spectra while the FTOOL "SISRMG" was used to prepare RMFs for the extracted SIS source spectra. Finally, the FTOOL "ASCAARF" was used to prepare ancillary response files (ARFs) for each extracted GIS and SIS source spectra.

2.2. Chandra Observation of CTB 1

We have also analyzed an archival data set from an additional X-ray observation of CTB 1 made with *Chandra* (Weisskopf et al. 2002). The corresponding ObsID of this observation is 2810 (PI: S. Kulkarni) and it was conducted as part of a search for central X-ray sources associated with Galactic SNRs. This observation was conducted in FAINT Mode on 2002 September 14 with the Advanced CCD Imaging Spectrometer (ACIS) at a focal plane temperature of -120°C such that the ACIS-I array of chips sampled a significant portion of the X-ray-emitting plasma located interior to the radio shell of the SNR. The ACIS-I array is composed of four front-illuminated CCD chips: each chip is $8.'3 \times 8.'3$ and the field of view of the entire array is approximately $17' \times 17'$. These chips are nominally sensitive to photons in the 0.2 through 10 keV energy range: the maximum effective collecting area for each chip is approximately 525 cm^2 at 1.5 keV. The FWHM angular resolution of each chip at 1 keV is $1''$ and finally the spectral resolution at 1 keV of each chip is 56. These data were reduced using the *Chandra* Interactive Analysis of Observations (CIAO[8]) package (Version 3.1) with the calibration database (CALDB) version 2.29. Standard processing was applied to this data set: in particular, the task "acis_process_events" was used to generate a new event file where corrections for charge transfer inefficiency and time-dependent gain were applied. The data were also filtered for bad pixels, background flare activity and events which had a GRADE value of 1, 5, or 7. Finally, we applied the good time interval (GTI) file supplied by the pipeline (as well as the GTI file prepared when filtering for background flares) and the resulting total effective exposure time of the observation was 48.9 ks.

Discrete sources were identified with the CIAO wavelet detection routine "wavdetect" (Freeman et al. 2002): in making a final image, these sources were excluded and the image was exposure-corrected and smoothed with the CIAO task "csmooth." We extracted spectra from several regions of the diffuse X-ray emission seen in the *Chandra* images using the CIAO task "dmextract": results of the spectral analysis are presented in Section 3.2. When extracting spectra, we excluded point sources identified by "wavdetect" to help reduce confusion with emission from background sources. We prepared ARFs and RMFs using the CIAO tools "mkwarf" and "mkrmf," respectively; background spectra were generated using a reprojected blank-sky observation made with the ACIS-I array and available from the *Chandra* X-ray Center via the World Wide Web.[9]

2.3. Additional Observations

We also included *ROSAT* Position Sensitive Proportional Counter (PSPC) observations of HB21 in our analysis: these observations were discussed already in some detail in the PhD thesis of Rho (1995). They extend beyond the two fields observed by *ASCA* and provide the complete spatial coverage of the SNR. The PSPC images are exposure and particle background corrected and merged together using the analysis techniques for extended objects developed by Snowden et al. (1994). The smoothing technique includes neighboring pixels within a circle of increasing radius until a selected number of counts is reached to optimize the signal-to-noise ratio.

Lastly, we have augmented the X-ray data sets analyzed in this work with radio data provided by the Canadian Galactic Plane Survey (CGPS; Taylor et al. 2003). From this survey, we have obtained radio images of HB21 and CTB 1 at the frequencies of 408 MHz and 1420 MHz, respectively. The angular resolution and sensitivity of the 408 MHz data are $3.'4 \times 3.'4$ csc δ and 0.75 sin δ K (3.0 mJy beam^{-1}), respectively, while the angular resolution and sensitivity of the 1420 MHz data are $1' \times 1'$ csc δ and 71 sin δ K (0.3 mJy beam^{-1}), respectively. The reader is referred to Taylor et al. (2003) for more description about the CGPS radio observations and the accompanying data reduction process.

3. RESULTS

3.1. HB21

In Figure 1, we present our broadband (0.7–10.0 keV) exposure-corrected mosaicked *ASCA* GIS image of HB21: we have overlaid radio emission contours using CGPS observations at a frequency of 408 MHz to show the extent of the SNR radio shell. In Figure 2, we present a mosaicked *ROSAT* PSPC image of HB21 (with the same radio contours overlaid), which depicts the entire extent of X-ray emission from the SNR (which extends

[7] See http://heasarc.gsfc.nasa.gov.
[8] http://cxc.harvard.edu/ciao/
[9] See http://cxc.harvard.edu/contrib/maxim/acisbg/.

Table 1
Summary of *ASCA* GIS and SIS Observations of HB21 and CTB 1

Sequence Number	SNR	Pointing	Observation Date	Right Ascension (J2000.0)	Declination (J2000.0)	GIS2 Effective Exposure Time (s)	GIS2 Count Rate (10^{-2} counts s^{-1})	GIS3 Effective Exposure Time (s)	GIS3 Count Rate (10^{-2} counts s^{-1})	SIS0 Effective Exposure Time (s)	SIS0 Count Rate (10^{-2} counts s^{-1})	SIS1 Effective Exposure Time (s)	SIS1 Count Rate (10^{-2} countss^{-1})
55053000	HB21	NW	1997 Jun 9–10	20 44 53.8	+50 54 31	39254	7.38 ± 0.19	39248	7.31 ± 0.19	35307	6.78 ± 0.18	35158	5.55 ± 0.17
55054000	HB21	SE	1997 Jun 10–11	20 46 31.4	+50 38 43	38415	7.18 ± 0.19	38413	7.39 ± 0.19	34448	5.52 ± 0.17	33940	4.21 ± 0.16
54026000	CTB1	SW	1996 Jan 21	23 57 31.9	+62 25 20	58065	6.03 ± 0.15	58078	5.44 ± 0.14	53592	10.52 ± 0.15	53746	8.64 ± 0.13
54027000	CTB1	NE	1996 Jan 22	00 01 21.9	+62 38 52	41637	4.83 ± 0.16	41649	5.16 ± 0.17	...	...	...	...

Notes. The units of right ascension are hours, minutes, and seconds and the units of declination are degrees, arcminutes, and arcseconds. Count rates are for the energy range 0.6–10.0 keV.

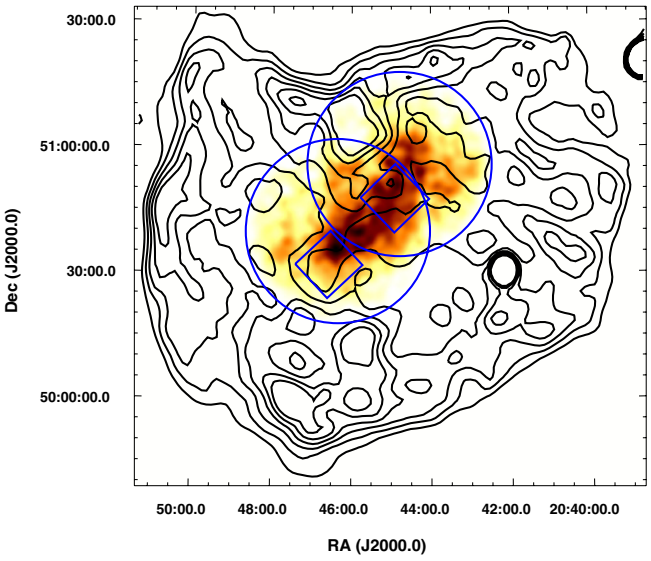

Figure 1. Mosaicked broadband *ASCA* GIS image of HB21: the emission has been smoothed with a 1′ FWHM Gaussian. The intensity range is (0–7.39) × 10^{-5} counts s^{-1} $arcmin^{-2}$. The contours represent radio emission from HB21 as observed at 408 MHz with the Canadian Galactic Plane Survey; they range from 0.445 Jy to 0.890 Jy per 3.′6 × 3.′6) in steps of 0.0445 Jy $beam^{-1}$. The blue boxes and circles represent the approximate fields of view of the *ASCA* SIS and the GIS, respectively.

(A color version of this figure is available in the online journal.)

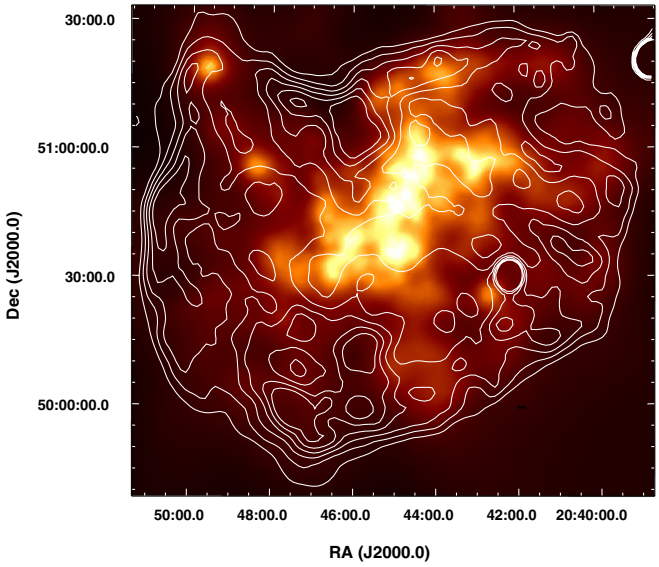

Figure 2. Mosaicked *ROSAT* PSPC image of HB21: we have superposed the same radio contours as in Figure 1. The intensity range of this image is 10^{-4}–2.1 × 10^{-2} counts s^{-1} $arcmin^{-2}$.

(A color version of this figure is available in the online journal.)

beyond the two fields observed by *ASCA*). It is clear from inspection of these images that the X-ray emission is located in the interior of the well-defined SNR radio shell: this combination of X-ray and radio morphologies exemplifies the defining characteristics of MM SNRs. The bulk of the interior X-ray-emitting plasma is located just south of a prominent bend in the northern edge of the radio shell. We note that Koo et al. (2001) detected broad CO emission lines from the location of this bend and Shinn et al. (2009) presented near- and mid-infrared images of this same region which showed shock–cloud interaction features. Both of these studies indicated that this is a site of an interaction between HB21 and a neighboring molecular cloud complex. In Figure 3, we present additional mosaicked *ASCA* GIS images which depict soft and hard emission (corresponding to the energy ranges of $E < 1$ keV and $E > 1$ keV, respectively) from this SNR. The GIS2 count rates for $E < 1$ keV and $E > 1$ keV are 1.91(±0.08) × 10^{-2} counts s^{-1} and 3.21(±0.15) × 10^{-2} counts s^{-1}, respectively, while the respective count rates for $E < 2$ keV and $E > 2$ keV are 4.56(±0.13) × 10^{-2} counts s^{-1} and 0.56(±0.08) × 10^{-2} counts s^{-1}. Significantly more X-ray emission is detected from HB21 at $E < 2$ keV X-ray energies than at $E > 2$ keV energies, illustrating the soft spectral nature typical of SNRs.

The GIS2/GIS3 spectra were extracted from elliptical regions approximately 23′ in size carefully selected to include most of the emission and avoid the edges of the field of view. Likewise, the SIS0/SIS1 spectra were extracted from square-shaped regions approximately 10 arcmin on a side and again the edges of the fields of view were avoided. We analyzed the extracted spectra using the software package *XSPEC*[10] Version 11.3.1 (Arnaud 1996). For our spectral fitting, we used two thermal models: the thermal model VAPEC, which describes an emission spectrum from a collisionally ionized diffuse gas with variable elemental abundances (Smith et al. 2000, 2001a, 2001b)[11], and VNEI, which is a non-equilibrium collisional plasma model which assumes a constant temperature and single ionization parameter (Hamilton et al. 1983; Liedahl et al. 1995; Borkowski et al. 2001). Photoelectric absorption along the line of sight was accounted for with the PHABS model; finally, we allowed the abundances of silicon and sulfur to vary during the fitting process (because lines associated with these particular elements are noticeable in the spectra) while leaving the abundances of the other elements frozen to solar values.

In Table 2, we present results of our simultaneous fits to the GIS2/GIS3 and SIS0/SIS1 spectra for both the northwestern and southeastern regions of HB21. We have obtained statistically acceptable fits (with χ^2_ν values of ∼1.04–1.06) to the extracted spectra using a single thermal component (that is, either the VAPEC model or the VNEI model) for both the northwestern and southeastern regions. The column density and temperature are similar for both thermal models, namely, $N_{\rm H} \sim$ (2–3) × 10^{21} cm^{-2} and $kT \sim 0.62$–0.68 keV. In Figure 4, we present the extracted GIS2, GIS3, SIS0, and SIS1 spectra for the northwest region of HB21: in each case, the fits obtained using ionization equilibrium (CIE) and non-equilibrium ionization models are comparable in quality. In addition, the abundances of silicon and sulfur in our spectral fits exceed solar abundances: these *ASCA* observations are the first to reveal enhanced abundances of heavy elements in the X-ray spectra of HB21 (as also noticed by Lazendic & Slane 2006). Our results are consistent with previous analyses of X-ray emission from HB21 (Leahy 1987; Rho 1995), where our present analysis of the broadband *ASCA* spectra has yielded similar temperatures to those derived from *Einstein* and *ROSAT* observations. However, with the data from the *ASCA* observations we may establish more stringent constraints on the ionization timescale and the abundances of sulfur and silicon. The ionization timescales derived with the VNEI model for the two regions are long ($\tau = 5.9$ (>3.2) × 10^{11} cm^{-3} s and $\tau = 4.1^{+5.9}_{-1.1} \times 10^{11}$ cm^{-3} s for the northwestern and southeastern regions of HB21, respectively)

[10] http://heasarc.gsfc.nasa.gov/docs/xanadu/xspec/

[11] Also see http://hea-www.harvard.edu/APEC.

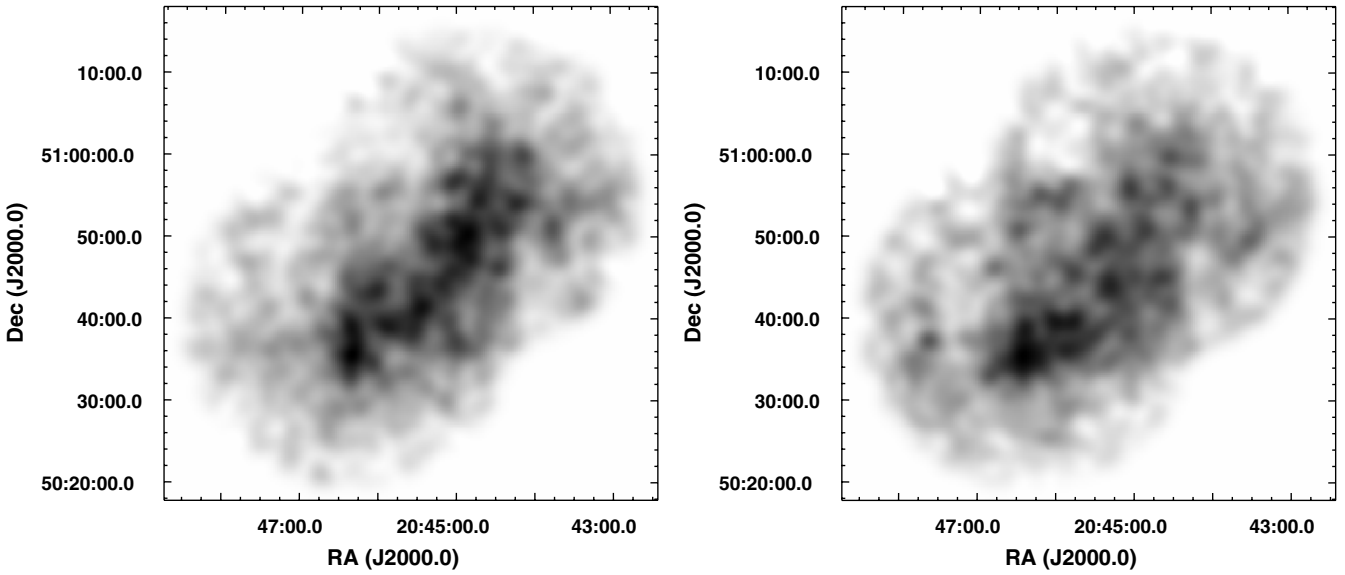

Figure 3. Mosaicked soft band ($E < 1$ keV—top) and hard band ($E > 1$ keV—bottom) GIS images of the central region of HB21: both images have been smoothed with a 1′ FWHM Gaussian. The coverages of the GIS images are marked in Figure 1. The intensity ranges of the two images are (0–1.02) $\times 10^{-4}$ and (0–2.58) $\times 10^{-5}$ counts s^{-1} arcmin^{-2}, respectively.

Table 2
Summary of Fits to GIS and SIS Spectra of HB21[a]

Parameter	GIS2/3+SIS0/1	GIS2/3+SIS0/1	GIS2/3+SIS0/1	GIS2/3+SIS0/1	GIS2	GIS2
Region	Northwest	Northwest	Southeast	Southeast	Northwest and Southeast	Northwest and Southeast
Model[b]	PHABS × VAPEC	PHABS × VNEI	PHABS × VAPEC	PHABS × VNEI	PHABS × VAPEC	PHABS × VNEI
χ^2_ν (χ^2/dof)	1.05 (1103/1054)	1.05 (1102/1053)	1.06 (1119/1054)	1.04 (1099/1053)	1.06 (340.43/321)	1.05 (336.50/327)
$N_{\rm H}$ ($\times 10^{22}$ cm^{-2})	0.23 ± 0.04	$0.24^{+0.06}_{-0.04}$	0.31 ± 0.04	0.30 ± 0.06	$0.22^{+0.05}_{-0.06}$	0.24 ± 0.06
kT (keV)	0.65 ± 0.03	$0.63^{+0.03}_{-0.04}$	$0.68^{+0.03}_{-0.02}$	0.67 ± 0.04	0.63 ± 0.06	$0.62^{+0.06}_{-0.05}$
Si	$1.3^{+0.3}_{-0.2}$	1.8 ± 0.5	1.4 ± 0.3	2.0 ± 0.4	$1.6^{+0.5}_{-0.3}$	$1.9^{+0.5}_{-0.4}$
S	2.4 ± 1.0	$3.6^{+1.7}_{-1.9}$	$1.7^{+0.9}_{-0.8}$	3.0 ± 1.4	$3.4^{+1.6}_{-1.4}$	$4.3^{+1.9}_{-1.8}$
τ (10^{11} cm^{-3} s)	...	5.9(>3.2)	...	$4.1^{+5.9}_{-1.1}$	...	350(>4.0)
EM[c] $/(4\pi d^2/10^{-14})$ (cm^{-5})	4.4×10^{-3}	4.4×10^{-3}	4.7×10^{-3}	4.4×10^{-3}	4.0×10^{-3}	4.5×10^{-3}
Absorbed flux[d] (erg cm^{-2} s^{-1})	5.2×10^{-12}	5.1×10^{-12}	4.7×10^{-12}	4.6×10^{-12}	5.1×10^{-12}	5.0×10^{-12}
Unabsorbed flux[d] (erg cm^{-2} s^{-1})	1.1×10^{-11}	1.1×10^{-11}	1.1×10^{-11}	1.1×10^{-11}	9.8×10^{-12}	1.1×10^{-11}
Unabsorbed luminosity[d] (erg s^{-1})	3.8×10^{33}	3.8×10^{33}	3.8×10^{33}	3.8×10^{33}	3.4×10^{33}	3.7×10^{33}

Notes.
[a] All quoted error bounds are 90% confidence intervals.
[b] PHABS is a photoelectric absorption model, VAPEC is a thermal plasma model in ionization equilibrium, and VNEI is a non-equilibrium ionization thermal model (see Section 3.1 for references for these models).
[c] Emission measure, defined here as $\int n_e n_{\rm H} dV$: here, d is the distance to HB21 (in cm) and n_e and $n_{\rm H}$ are the electron and H densities (in cm^{-3}).
[d] For the energy range 0.6–10.0 keV. The luminosity estimates are for an assumed distance of 1.7 kpc.

and within the error bounds for this parameter, CIE is included ($\tau \geqslant 10^{12}$ cm^{-3} s; see Smith & Hughes 2010). For this reason and because both the VAPEC and VNEI models return equally acceptable fits, we argue that the X-ray-emitting plasma located within the interior of HB21 is close to ionization equilibrium. Similar to the results presented by Lazendic & Slane (2006), we also observed slightly enhanced silicon and sulfur abundances in HB21: based on our PHABS×VAPEC (PHABS×VNEI) fits, our measured abundances are Si $= 1.3^{+0.3}_{-0.2}$ (1.8 ± 0.05) and S $= 2.4 \pm 1.0$ ($3.6^{+1.7}_{-1.9}$) for the northwestern region and Si $= 1.4 \pm 0.3$ (2.0 ± 0.4) and S $= 1.7^{+0.9}_{-0.8}$ (3.0 ± 1.4) for the southeastern region (see Table 2). The slightly different abundances between the VAPEC and VNEI fits may be due to either differences in the predicted line strengths between the non-equilibrium and equilibrium conditions or different sets of atomic data incorporated in these models. The respective lower limits for the abundances of Si (S) for the northwestern region are 1.1 (1.3) and 1.4 (1.7), while the lower limits for the southeastern region are 1.1 (1.6) and 0.9 (1.6). The northwestern region shows modestly more consistent evidence of slightly enhanced silicon and sulfur abundances than the southeastern region. This suggests a contribution to the observed X-ray spectra from ejecta material.

In Figure 5, we present a plot of confidence contours for the silicon and sulfur abundances based on the PHABS×VAPEC fit to the spectrum of the northwestern region. No significant spectral differences are seen between the northwestern and southeastern regions of this SNR. In their analysis of spectra extracted from the *ASCA* observations of HB21, Lazendic & Slane (2006) found that fits obtained using the VNEI model to the spectra extracted for both regions gave better fits at a

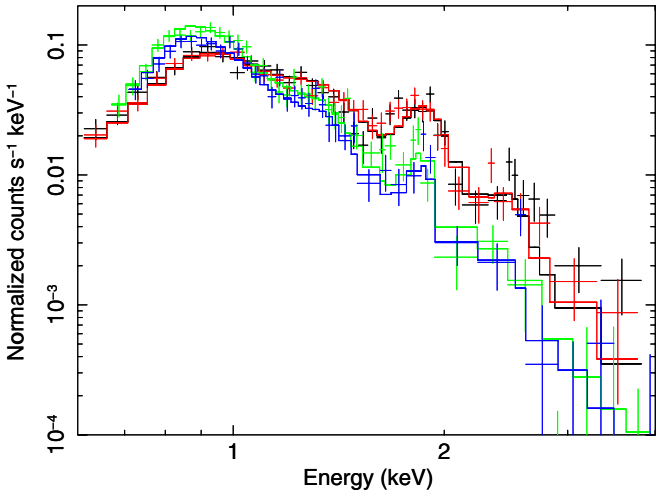

Figure 4. GIS2 (red), GIS3 (black), SIS0 (green), and SIS1 (blue) spectra of the northwestern portion of HB21 superposed on PHABS×VNEI models (see Table 2).

(A color version of this figure is available in the online journal.)

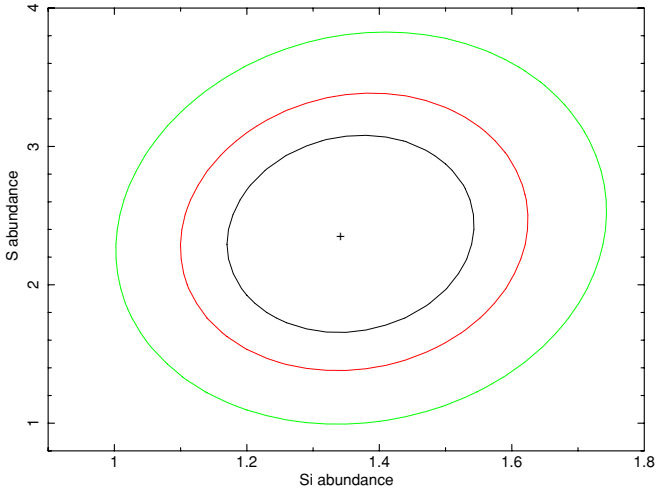

Figure 5. Confidence contours for the abundances of Si and S for the PHABS×VAPEC fit to the extracted GIS2, GIS3, SIS0, and SIS1 spectra of the northwestern portion of HB21. The confidence contours are at the 1σ, 2σ, and 3σ levels (see Table 2).

(A color version of this figure is available in the online journal.)

statistically significant level (4σ) than fits obtained by a thermal plasma. In contrast, we find that fits obtained with VNEI and fits obtained with a standard thermal plasma are comparable in quality. Also, Lazendic & Slane (2006) derived comparable (though slightly larger) values for $N_{\rm H}$ for both regions: those authors also found a similar trend where $N_{\rm H}$ is modestly elevated for the southeastern region compared to the northwestern region. We suspect that the minor differences between our results and those obtained by Lazendic & Slane (2006) may be attributed to small differences in data reduction and spectral analysis techniques (such as background subtraction). We also point out that Lazendic & Slane (2006) commented that the derived column density values seemed to be rather high if HB21 is indeed only 0.8 kpc distant (which was their assumed distance to the SNR). They noted that an elevated column density (at least for the eastern portion of the SNR) is comparable to the column density of the complex of molecular clouds seen toward HB21 as described by Tatematsu et al. (1990). We notice that if the larger distance to HB21 that we have assumed

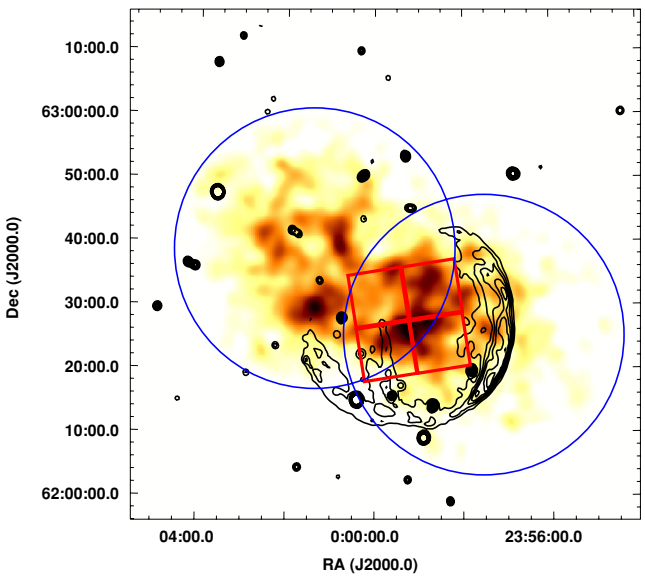

Figure 6. Mosaicked broadband *ASCA* GIS image of CTB 1 (color): the emission has been smoothed with a 1′ FWHM Gaussian. The intensity range is (0–5.93) × 10^{-5} counts s^{-1} arcmin^{-2}. The contours represent radio emission as observed at 408 MHz with the Canadian Galactic Plane Survey (CGPS): the contours range from 0.024 Jy to 0.063 Jy per 0.′9 × 0.′9 in steps of 0.0035 Jy beam^{-1}. The blue circles depict the approximate fields of view of the *ASCA* GISs while the red squares depict the approximate fields of view of the *Chandra* ACIS-I chips.

(A color version of this figure is available in the online journal.)

(1.7 kpc) is adopted, the measured values for $N_{\rm H}$ seem more reasonable.

Lastly, to help determine more stringent constraints on the properties of the X-ray-emitting plasma (specifically the abundances of silicon and sulfur), we simultaneously fit the GIS2 spectra extracted for the northwestern and southeastern portions of the SNR with first the PHABS×VAPEC model and then with the PHABS×VNEI model. For both models, we obtained statistically acceptable fits (with χ^2_ν values of $\sim$1.1) with values for kT and $N_{\rm H}$ that were consistent with those obtained for fits of the individual regions (that is, $kT \sim 0.6$ keV and $N_{\rm H} \sim 0.2 \times 10^{22}$ cm^{-2}). The abundances for both silicon and sulfur were indeed enhanced relative to solar: for the PHABS×VAPEC (PHABS×VNEI) model, the abundances were 1.7 ± 0.4 ($1.9^{+0.5}_{-0.4}$) for silicon and $3.5^{+1.9}_{-1.0}$ ($4.3^{+2.2}_{-1.8}$) for sulfur. The ionization timescale derived for the PHABS×VNEI model—$\tau \sim 4(>0.03) \times 10^{13}$ cm^{-3} s—is also consistent with ionization equilibrium. We summarize the results for these fits in Table 2.

3.2. CTB 1

A broadband (0.7–10.0 keV) exposure-corrected and mosaicked *ASCA* GIS image of CTB 1 is presented in both Figures 6 and 7 with radio contours from the CGPS overlaid. Both HB21 and CTB 1 show the typical center-filled X-ray morphology combined with a shell-like radio morphology that characterizes MM SNRs: in the case of CTB 1, however, as noted previously the X-ray emission is seen to extend through a gap along the northeastern portion of the radio shell. Figure 8 shows mosaicked images of the soft and hard X-ray emission (again corresponding to the energy ranges $E < 1$ keV and $E > 1$ keV, respectively); there is a noticeable difference in the spatial structure between the soft and the hard emission. In Figure 9, we present an optical Hα image of CTB 1 (courtesy of

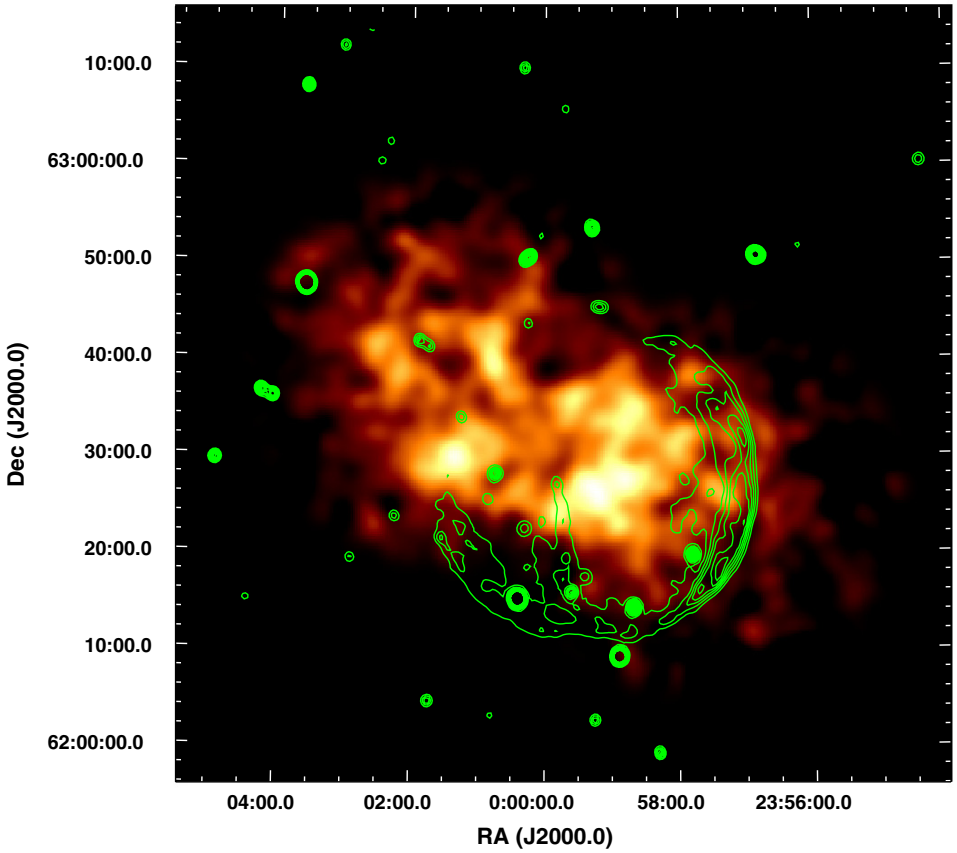

Figure 7. *ASCA* GIS image of CTB 1 with CGPS radio contours overlaid: these radio contours are at the same levels as those shown in Figure 6.
(A color version of this figure is available in the online journal.)

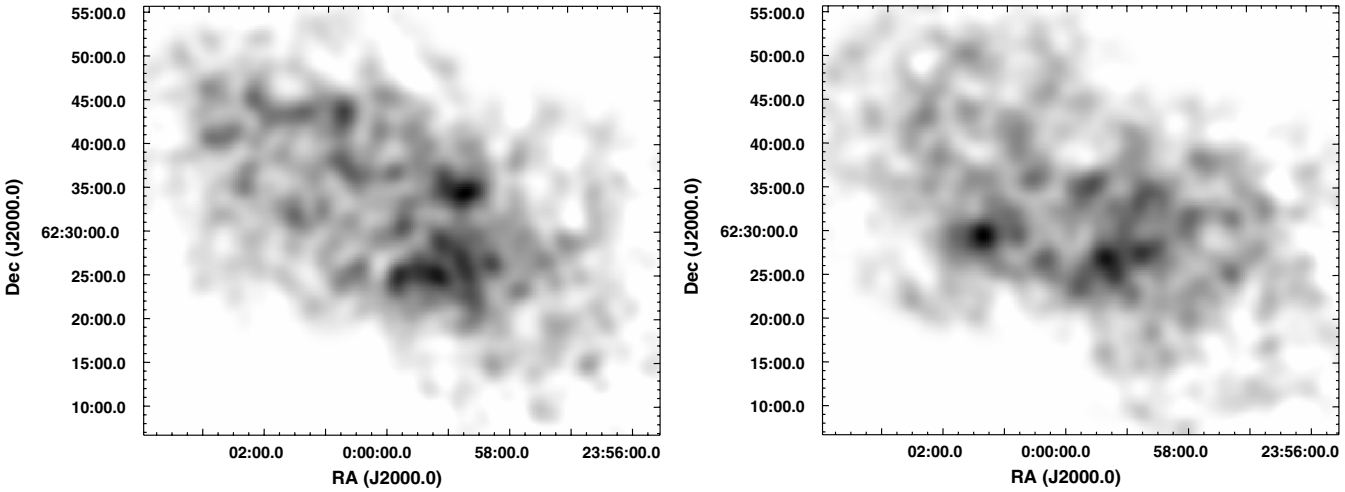

Figure 8. Mosaicked soft band ($E < 1$ keV—left) and hard band ($E > 1$ keV—right) GIS images of CTB 1: both images have been smoothed with a 1′ FWHM Gaussian. The intensity ranges are (0–6.42) $\times 10^{-5}$ and (0–2.85) $\times 10^{-5}$ counts s^{-1} arcmin^{-2}, respectively. The discrete source 1WGA J0001.4 + 6229 (located at R.A. (J2000.0) $00^{h}01^{m}25\overset{s}{.}5$, decl. (J2000.0) +62°29′40″) becomes more prominent at higher energies: this source is discussed in detail in Section 4.

Robert Fesen) with the contours of the X-ray emission overlaid: the optical morphology of CTB 1 is quite similar to the radio morphology with the same shell-like structure and a prominent gap in the northeast (Fesen et al. 1997). Little Hα emission is seen in the interior of CTB 1, nor is any optical emission seen where the X-ray emission extends through the gap in the optical and radio shell in the northeast. The observed slight extension of X-ray emission in the west through the optical and radio shell is likely either residuals due to the broad *ASCA* point-spread function or point sources rather than true emission from the SNR. The *ASCA* hard image reveals a point-like source seen in projection against the diffuse emission of CTB 1: it is located at R.A. (J2000.0) $00^{h}01^{m}25\overset{s}{.}5$, decl. (J2000.0) +62°29′40″ and it lies very close to the eastern edge of the optical and radio shell. This source (denoted as 1WGA J0001.4+6229) may be a neutron star possibly associated with CTB 1; we discuss it in detail in the next section. In contrast to HB21, a significant amount of emission from CTB 1 is seen at energies above 1 keV.

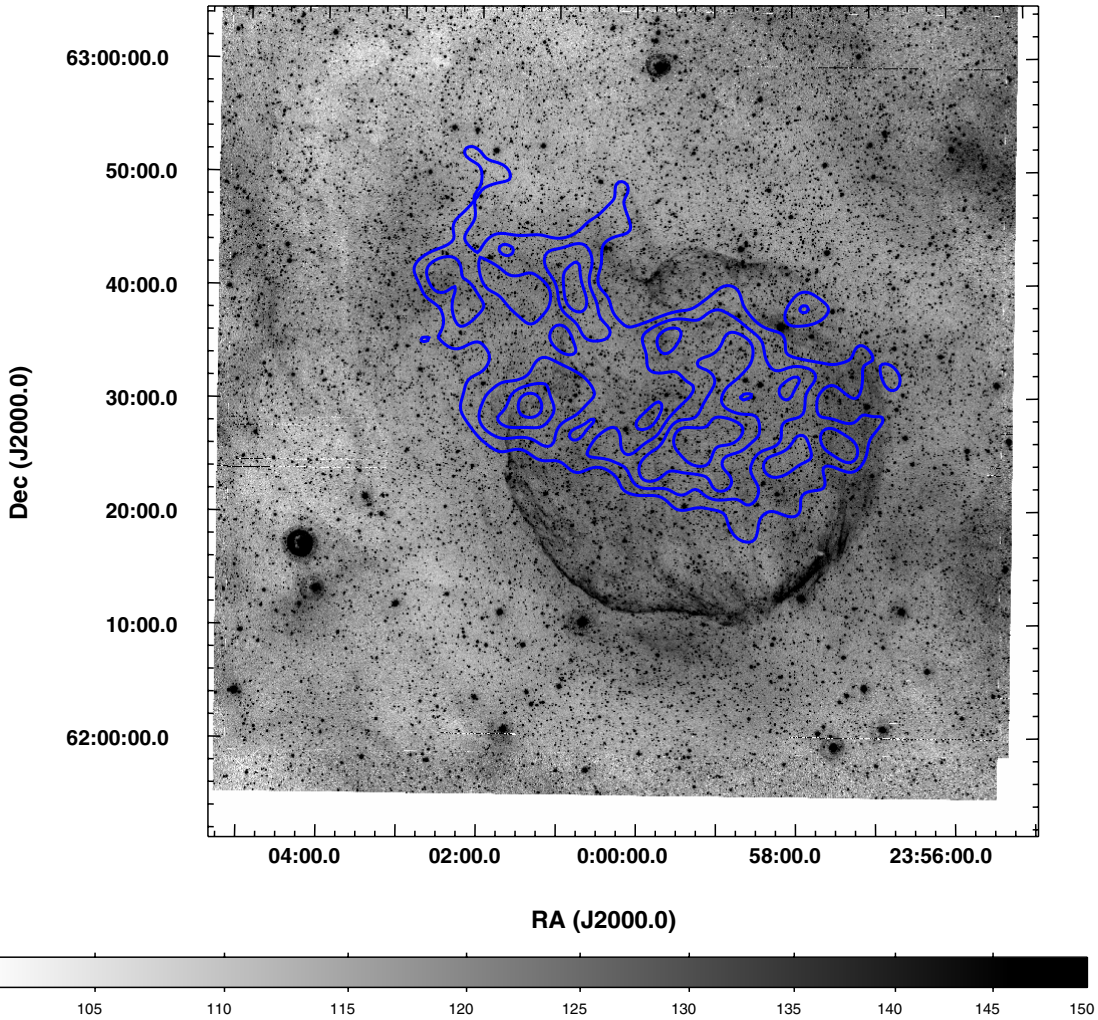

Figure 9. Hα image of CTB 1 in gray scale (courtesy of Robert Fesen) with blue *ASCA* GIS contours overlaid. The contour levels are 2.05, 3.04, 4.02, and 5.01 $\times$ 10^{-5} counts s^{-1} arcmin^{-2}. Note how the X-ray emission extends through the prominent gap of optical emission.

(A color version of this figure is available in the online journal.)

Similar to our spectral analysis performed with HB21, we extracted GIS2 and GIS3 spectra from elliptical regions approximately 23′ in size from both the southwestern and northeastern portions of the X-ray-emitting plasma. When extracting GIS2 and GIS3 spectra from the northeastern region, we excluded a region 4 arcmin in diameter centered on the position of the discrete X-ray source 1WGA J00001.4+6229 to avoid spectral contamination by this source. We also extracted SIS0 and SIS1 spectra from both the southwestern and northeastern portions of the SNR, again using square-shaped regions approximately 10 arcmin on a side. Unfortunately, the signal-to-noise ratio of the extracted SIS0 and SIS1 spectra for the northeastern region was not sufficient for spectral analysis and we therefore omitted these spectra from our study. We attempted to fit the extracted *ASCA* spectra using the thermal models VAPEC and VNEI along with the model PHABS for the photoelectric absorption. In contrast to HB21, our fits with either VAPEC or VNEI *did not* produce a χ^2_ν lower than 1.3 for either region and failed to account for the hard X-ray emission seen above $\sim$3 keV from both regions. A two-component model with a soft thermal component with a temperature of 0.3–0.4 keV (either VAPEC or VNEI) and a second thermal component with a higher temperature or a power-law component was required for an acceptable fit to the extracted spectra from both the southwest and northeast portions of the SNR (see Table 4). Thus, a hard excess is present in the *ASCA* spectra of CTB 1: Lazendic & Slane (2006) also identified a second thermal component of X-ray emission from this SNR based on analysis of extracted *ASCA* spectra but only for the southwestern region. This hard X-ray emission was not detected previously because the X-ray observatories employed in prior observations of CTB 1 (such as *ROSAT*) lacked the required sensitivity at high energies.

We examine first the high spatial resolution *Chandra* data before discussing the hard emission in more detail. In Figure 10, we present a three-color *Chandra* image of the interior X-ray emission surrounded by the well-defined optical and radio shell of CTB 1. To illustrate the spectral properties of this emission, in this figure, we have depicted soft (0.5–1.0 keV), medium (1.0–2.0 keV), and hard (2.0–8.0 keV) emission in red, green, and blue, respectively. Many features with different spectral properties are visible: most importantly, features with primarily medium and hard spectra are clearly mixed together within the X-ray plasma. At the angular resolution of *Chandra*, the hard emission (such as the structure $\sim$ 1 arcmin in size located at approximately R.A. (J2000.0) $23^{\rm h}59^{\rm m}01\overset{\rm s}{.}0$, decl. (J2000.0) $+62^\circ30'57''$) is clearly diffuse and not point like.

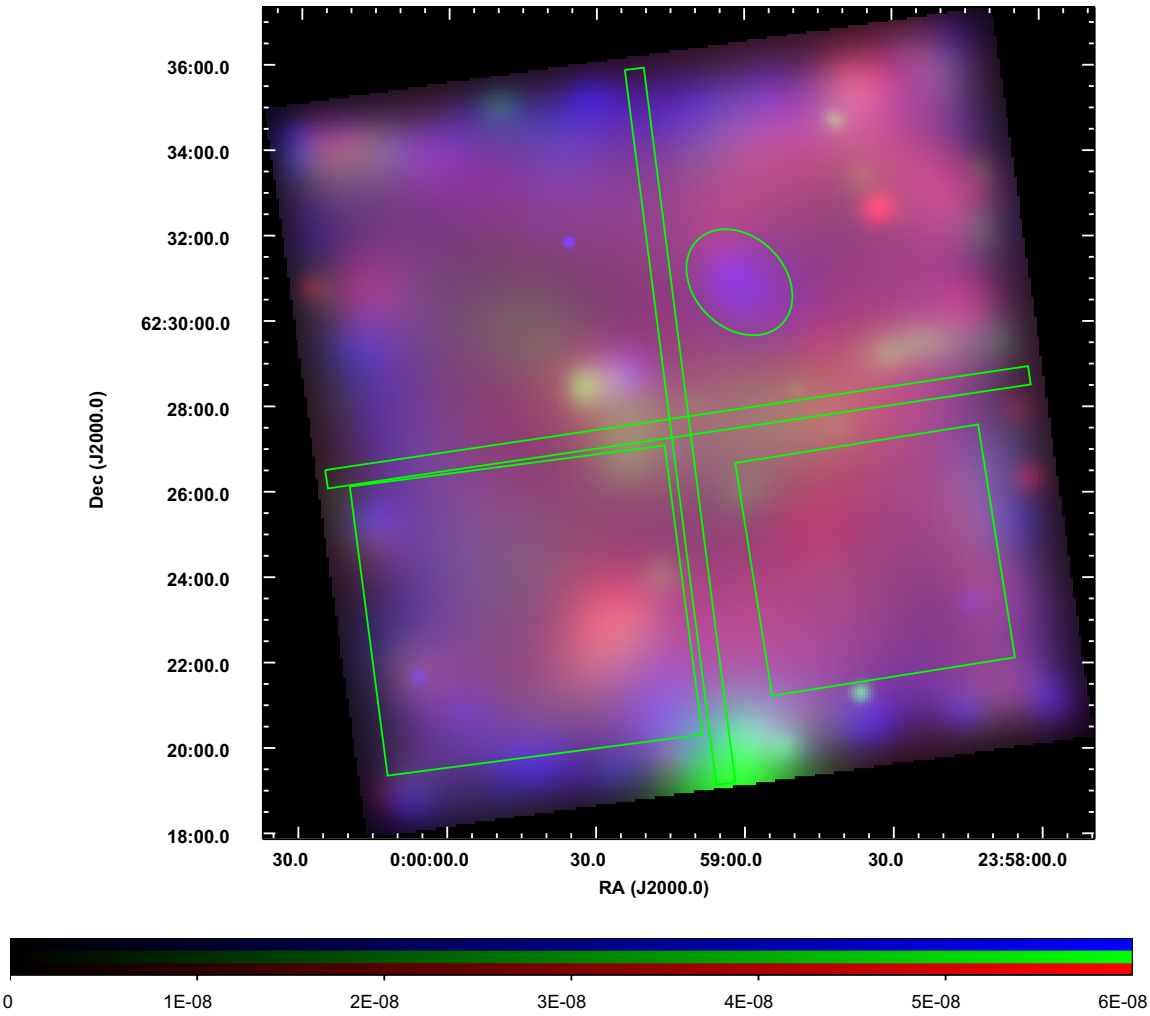

Figure 10. Three-color exposure-corrected and smoothed *Chandra* image of the interior of CTB 1. This image has been made using monoenergetic exposure maps. Red, green, and blue colors correspond to soft (0.5–1.0 keV), medium (1.0–2.0 keV), and hard (2.0–8.0 keV) emission, respectively. The three regions (in green) of spectral extraction are indicated: clockwise from upper left, these are the regions denoted as "hard," (I1 chip), "soft" (I3 chip), and "diffuse" (I2 chip) excluding point sources (see Section 3.2). The boundaries of the *Chandra* chips are marked with thin boxes (in green). Note how clumpy features with different spectral properties can be distinguished by noticeable differences in their colors. See Section 3.2.

(A color version of this figure is available in the online journal.)

To investigate variations in the spectral properties of the X-ray-emitting plasma of CTB 1 as revealed by *Chandra*, we extracted spectra from three different *Chandra* chips. These three extraction regions are as follows: the first region (which we refer to as the "diffuse" region) is on the ACIS-I2 chip and covers most of the area of this chip. A second region (which we refer to as the "soft" region) is located on the ACIS-I3 chip and covers most of the area of that chip as well. Lastly, we extracted spectra from a third region (which we will call the "hard" region) which corresponds to a region of hard emission mentioned above and is located on the ACIS-I1 chip: the positions of all three regions are indicated in Figure 10. A region of excess medium energy seen toward the middle of the field in Figure 10 largely fell into gaps between the *Chandra* detector chips: for this reason, a detailed analysis of its X-ray spectrum could not be conducted.

We present the extracted spectra of all three regions in Figure 11: spectral variations are present across the X-ray-emitting plasma of CTB 1. For example, the spectrum from the "diffuse" region shows prominent O Lyα (0.65 keV), Ne IX (0.9 keV), and Mg XIII (1.35 keV) lines, together with Fe L-shell line emission: in this spectrum, the O and Ne lines are stronger than the Fe L-shell line emission. In contrast, the lines are hardly noticeable in the "hard" region spectrum. We derived an acceptable fit to the spectrum of the diffuse region using a thermal model (VAPEC) with a temperature $kT = 0.28 \pm 0.03$ keV and $N_{\rm H} = 0.64 \pm 0.08 \times 10^{22}$ cm^{-2}; this fit reveals enhanced oxygen and neon abundances and a low iron abundance (see Table 3). The column density $N_{\rm H} = 0.64 \pm 0.08 \times 10^{22}$ cm^{-2} is consistent with the optical extinction of $E(B - V) = 0.7$–1 derived by Fesen et al. (1997), which is equivalent to $N_{\rm H} \sim 0.5$–0.7×10^{22} cm^{-2}. In Figures 12(a) and (b), we present confidence contour plots for the abundances of oxygen compared to iron and neon compared to iron (respectively) based on the fit derived from the PHABS$\times$VAPEC model to the spectrum of the "diffuse" region. These figures show that the oxygen and neon abundances are both above solar while the iron abundance is below solar: such relative abundances are a typical characteristic of oxygen-rich SNRs (Woosley & Weaver 1995).

Our detection and analysis presented here of probable oxygen-rich ejecta in CTB 1 is the first detailed study presented of oxygen-rich ejecta associated with an MM SNR. Based on

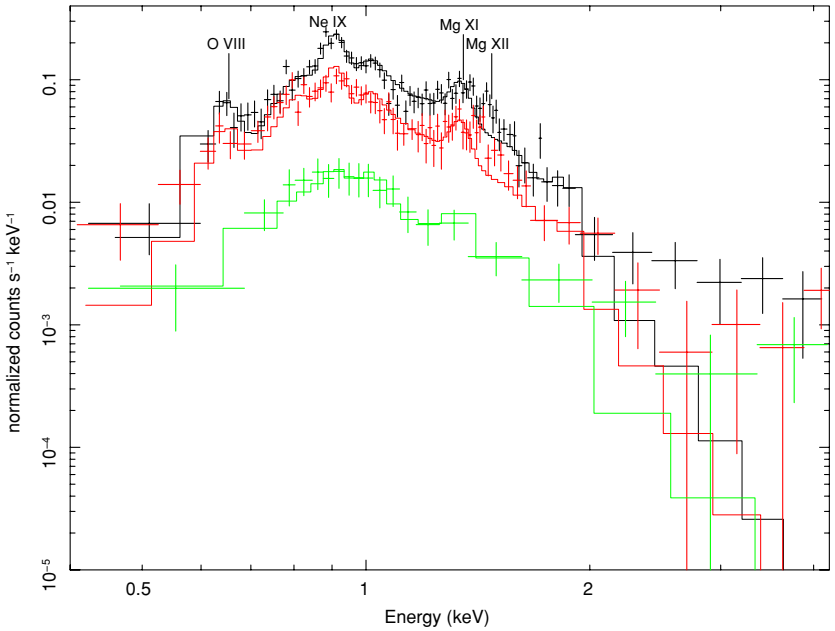

Figure 11. *Chandra* spectra of the three different regions of CTB 1. The black, red, and green lines correspond to spectra from the "diffuse," "soft," and "hard" regions, respectively. The spectra have been fit with a PHABS×VAPEC model with the temperature of 0.28, 0.28, and 0.66 keV, respectively. The detailed parameters for these fits are given in Table 3.

(A color version of this figure is available in the online journal.)

Table 3
Summary of Fits to *Chandra* Spectra of CTB 1[a]

Parameter	Diffuse Region	Soft Region	Hard Region	Hard Region	Hard Region
Model	PHABS × VAPEC	PHABS × VAPEC	**PHABS × VAPEC**	PHABS × POWER LAW	PHABS × (APEC+POWER LAW)
χ^2_ν (χ^2/dof)	0.99 (169.72/172)	0.94 (122.77/131)	0.41[d] [0.41][e]	0.50[d]	0.40[d]
$N_{\rm H}$ ($\times 10^{22}$ cm^{-2})	0.64 ± 0.08	$0.56^{+0.11}_{-0.16}$	$0.18(<0.75)$ $[0.36^{+0.39}_{-0.25}]$	$0.76(^{+0.64}_{-0.57})$	0.47(–)
kT_1 (keV)	0.28 ± 0.03	$0.28^{+0.06}_{-0.04}$	$0.66^{+0.27}_{-0.41}$ $[0.63^{+0.17}_{-0.53}]$	···	0.28 (frozen)
O	$1.7^{+1.2}_{-0.6}$	$1.8^{+2.2}_{-0.8}$	1.7 [≡1]	···	1 (frozen)
Ne	$1.6^{+0.8}_{-0.5}$	$1.1^{+1.0}_{-0.4}$	$1.1^{+1.0}_{-0.4}$ [≡1]	···	1 (frozen)
Fe	0.4 ± 0.2	$0.7^{+0.6}_{-0.3}$	$0.5^{+3.0}_{-0.3}$ [≡1]	···	1 (frozen)
EM_1[b]$/(4\pi d^2/10^{-14})$ (cm^{-5})	4.33×10^{-3}	2.23×10^{-3}	2.14×10^{-4}	···	2.41×10^{-4}
Γ	···	···	···	$6.4(^{+5.6}_{-2.9})$	1.9(–)
Normalization	···	···	···	2.08×10^{-4}	1.27×10^{-5}
Counts[c]	9232	5319	979	979	979
Absorbed flux[c] (erg cm^{-2} s^{-1})	5.29×10^{-13}	3.62×10^{-13}	5.90×10^{-14}	6.50×10^{-14}	8.21×10^{-14}
Unabsorbed flux[c] (erg cm^{-2} s^{-1})	8.66×10^{-12}	4.70×10^{-12}	7.52×10^{-13}	1.60×10^{-12}	4.34×10^{-13}
Luminosity[c] (erg s^{-1})	9.96×10^{33}	5.41×10^{33}	8.65×10^{32}	1.84×10^{33}	4.99×10^{32}

Notes.
[a] All quoted error bounds are 90% confidence intervals. The best model is marked in bold where a few models are presented for the same spectra set.
[b] Defined as $\int n_e n_{\rm H}\, dV$: here, d is the distance to CTB 1 (in cm) and n_e and $n_{\rm H}$ are the electron and H densities (in cm^{-3}).
[c] For the energy range 0.5–5.0 keV.
[d] The number of degrees of freedom for these fits ranges from 101 to 104.
[e] The numbers in brackets are the fits with fixed solar abundances.

X-ray spectral analysis, Lazendic & Slane (2006) suggested that another MM SNR—HB 3—may also feature oxygen-rich ejecta, though those authors could not determine if the plasma associated with that SNR has significantly enhanced abundances of oxygen, neon, and magnesium or marginally enhanced abundances of magnesium and underabundant iron. The *Chandra* spectra are not well fit by a single temperature thermal model (see the poor match to the Mg XII Lyα line as seen in Figure 3), so it is not possible to have oxygen, neon, and magnesium all residing in the same constant temperature plasma in ionization equilibrium. Magnesium appears to be more ionized than neon. This may be caused by higher temperatures in magnesium-rich ejecta than in the oxygen- and neon-rich ejecta. It is also possible that the high temperature plasma could be overionized; an overionized plasma has been reported in the MM SNR IC 443 (Kawasaki et al. 2002). When we fit the spectrum of the "soft" region using a VAPEC model combined with the PHABS model for the interstellar photoelectric absorption, the iron abundance is higher and the neon abundance is lower when compared with the "diffuse" region spectra (see Table 3), suggesting spatial variations in the chemical composition within the X-ray-emitting gas of CTB 1.

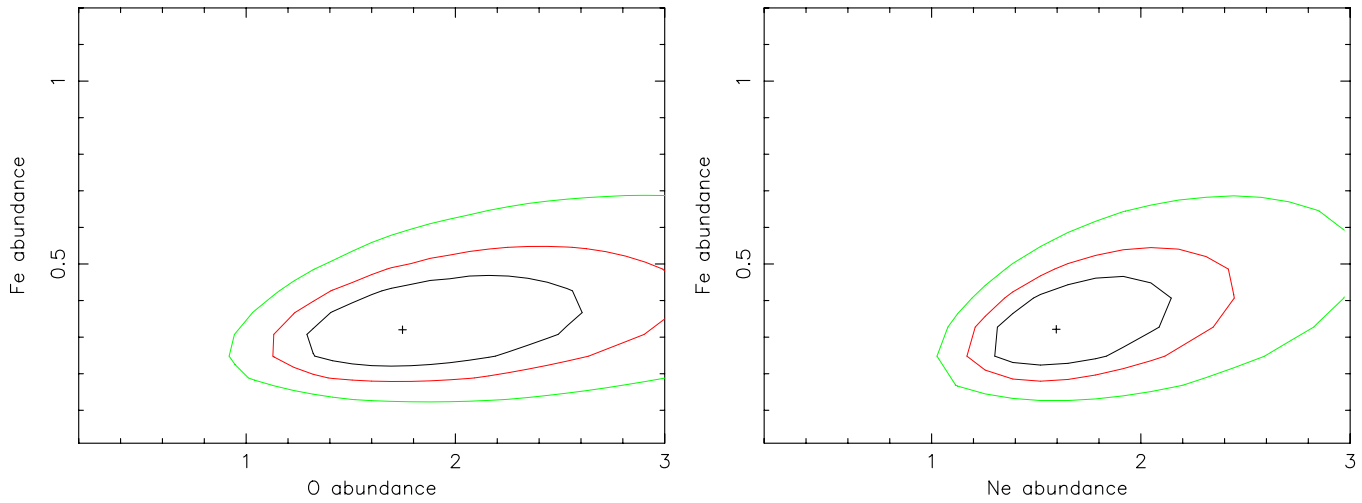

Figure 12. Confidence contours of (a) O and Fe abundances and (b) Ne and Fe abundances, respectively, showing enhanced O and Ne abundances and lower Fe abundance relative to solar, for the PHABS×VAPEC fit to the spectrum extracted for the "diffuse" region. The confidence contours are at the 1σ, 2σ, and 3σ levels. See Table 3.

(A color version of this figure is available in the online journal.)

Lastly, we describe the spectral analysis of the third ("hard") region, which features a harder spectrum when compared to the other two spectra (see Figure 11). Such localized hard emission has been reported in several other MM SNRs, either as non-thermal diffuse knots seen in *XMM-Newton* observations of IC 443 (Bocchino & Bykov 2003) or as a pulsar wind nebula (also in IC 443—Olbert et al. 2001). Because of the lack of lines in the spectrum, we first fit the spectra with a power law, which resulted in an acceptable fit, but with an unrealistically high photon index of $\Gamma \sim 6.4^{+5.6}_{-2.9}$ (see Table 3). In comparison, a VAPEC thermal model yielded a comparable-quality fit with a temperature of $kT = 0.66^{+0.27}_{-0.41}$ keV: for this fit, we froze the abundance of oxygen to 1.7 (to be consistent with the fits derived to the spectra of the "diffuse" and "soft" regions) or 1 while fitting for the abundances of neon and iron. We also fit the spectrum of this region with a combination of an APEC thermal component and a non-thermal power-law component; to reduce the number of free parameters, we fixed the temperature of the thermal component to $kT = 0.28$ keV, equal to the temperature derived from fits to the other two regions. The results are given in Table 3: unfortunately, we do not have enough counts in the spectrum of the "hard" region to distinguish between non-thermal and thermal interpretations of the spectrum of this source. However, the temperature derived from the thermal fit ($kT = 0.66$ keV) is significantly higher than the temperature of the "soft" and "diffuse" regions. Also, thermal models systematically underpredict *Chandra* spectra at high energies in all the regions: we interpret this result as evidence that the hard excess observed toward CTB 1 has a diffuse origin.

In Figure 13, we present a plot of confidence contours for $N_{\rm H}$ and kT that correspond to the fit to the spectrum of the "hard" region as fit with the PHABS×VAPEC model with fixed solar abundances. The spectrum of this region demonstrates a bimodality with temperatures of $kT \sim 0.28$ keV and $kT \sim 0.66$ keV, suggesting the presence of an additional component in addition to the thermal component associated with the "diffuse" region. We will discuss the nature of this hard component further below and in Section 7. We also note differences between our results from analyzing *Chandra* ACIS-I spectra and the results presented by Lazendic & Slane (2006): those authors jointly fit four spectra taken from each ACIS-I chip

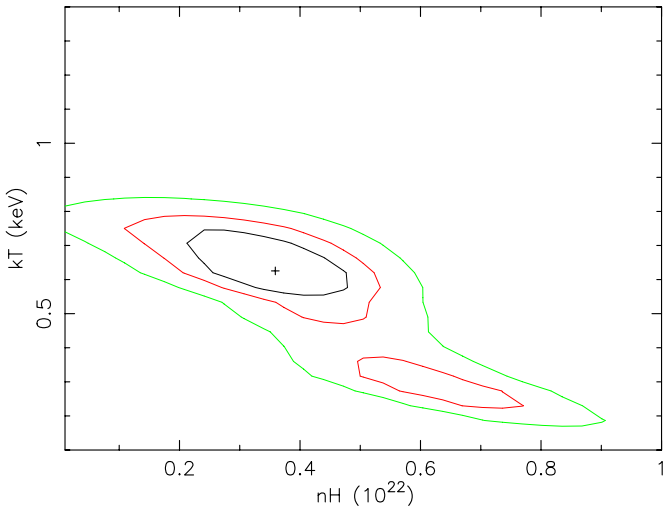

Figure 13. Confidence contours for the line-of-sight column density $N_{\rm H}$ and the temperature kT for the PHABS×VAPEC spectral fit (with fixed solar abundances) to the spectrum of the "hard" region (see Table 3). Note the bimodality for components with temperatures of $kT \sim 0.28$ keV and $kT \sim 0.66$ keV: this may indicate a presence of an additional thermal component besides the thermal component identified in the fit of the spectrum of the "diffuse" region. The confidence contours are at the 1σ, 2σ, and 3σ levels. See Section 3.2.

(A color version of this figure is available in the online journal.)

(they did not attempt any spectral analysis of small regions like the "hard" region") and presented an acceptable fit obtained using two VNEI components: one with a temperature $kT = 0.20^{+0.04}_{-0.01}$ keV and solar abundances and the other with a temperature $kT = 0.86^{+0.03}_{-0.06}$ and an elevated magnesium abundance (Mg $= 3.1^{+1.0}_{-0.4}$). Those authors did comment on the presence of lines associated with oxygen as well as the neon and iron lines blend in the extracted ACIS spectra but they did not present an analysis of the abundance of those elements.

After establishing the spectral properties of the soft X-ray-emitting plasma from *Chandra* spectra, we fit the *ASCA* GIS2/3 and SIS0/1 spectra of the southwestern portion of CTB 1. We froze the oxygen abundance to 1.7 (or 1) for all spectral fits while

Table 4
Summary of Fits to GIS and SIS Spectra of Southwest and Northeast Regions of CTB 1[a]

Parameter	GIS2/3+SIS0/1	GIS2/3+SIS0/1	GIS2/3+SIS0/1	GIS2/3+SIS0/1	GIS2/3+SIS0/1	GIS2/3+SIS0/1	GIS2/3
Region	Southwest	Southwest	Southwest	Southwest	Southwest	Southwest	Northeast
Model	PHABS × VAPEC	PHABS × VNEI	PHABS × (VAPEC+ POWER LAW)	**PHABS × (VNEI+ POWER LAW)**	PHABS × (VAPEC+ VAPEC)	**PHABS × (VNEI+ VNEI)**	PHABS × (VAPEC+ POWER LAW)
χ^2/dof	1.33[g] [1.33][h]	1.29	1.15 [1.15][g]	1.12[g] [1.19][h]	1.13[g]	1.12[g] [1.12][h]	1.19[i] [1.16][h]
$N_{\rm H}$ ($\times 10^{22}$ cm^{-2})	0.59 [0.51]	0.68	$0.55^{+0.13}_{-0.15}$	$0.57^{+0.48}_{-0.19}$ [0.59]	$0.66^{+0.09}_{-0.13}$	$0.80^{+0.3}_{-0.1}$ [0.9]	0.47 ± 0.32 [0.60]
$kT_{\rm soft}$ (keV)	0.30 [0.30]	0.41	$0.28^{+0.09}_{-0.04}$	$0.27^{+0.23}_{-0.15}$ [0.27]	$0.25^{+0.05}_{-0.03}$	$0.23^{+0.17}_{-0.06}$ [0.22]	$0.22^{+0.34}_{-0.12}$ [0.24]
O[b]	1.7 [≡1]	1.7	1.7	1.7 [≡1]	1.7	1.7 [≡1]	≡1.7 [≡1]
Ne	1.6 [1.2]	1.6	1.6	2.7(>2.0) [≡1]	2.1 ± 0.4	$2.0^{+0.5}_{-1.1}$ [1.8]	≡1.6 [≡1]
Fe	0.5 [0.4]	0.4	0.4	0.8(>0.4) [≡1]	0.7 ± 0.4	$1.2^{+3.8}_{-0.5}$ [1.2]	≡0.4 [≡1]
τ_1 (10^{11} cm^{-3} s)	...	2	...	10 (>0.2) [15]	...	0.4(<5) [0.4]	...
EM$_1$[c]/(4πd^2/10^{-14}) (cm^{-5})	2×10^{-2}	2×10^{-2}	2×10^{-2}	2×10^{-2}	3×10^{-2}	8×10^{-2}	2×10^{-2}
Γ or $kT_{\rm hard}$[d]	...	...	$2.2^{+0.4}_{-1.1}$	$3.0^{+1.8}_{-1.3}$ [3.0]	$3.3^{+4.7}_{-1.5}$	3.1(> 2) [3]	1.4 ± 0.9
τ_2 (10^{11} cm^{-3} s)	...	...	...	...	...	$0.7^{+1.2}_{-0.4}$ [0.7]	...
EM$_2$[c]/(4πd^2/10^{-14}) (cm^{-5})	...	...	...	1×10^{-3}	1×10^{-3}	8×10^{-4}	...
Normalization[e]	...	...	4×10^{-4}	...	...	...	2×10^{-4}
Absorbed flux[f]	3.52×10^{-12}	3.64×10^{-12}	4.44×10^{-12}	4.31×10^{-12}	4.38×10^{-12}	4.43×10^{-12}	4.37×10^{-12}
Unabsorbed flux[f]	3.37×10^{-11}	5.35×10^{-11}	3.34×10^{-11}	3.50×10^{-11}	4.88×10^{-11}	1.10×10^{-10}	3.02×10^{-11}
Luminosity[e]	3.88×10^{34}	6.16×10^{34}	4.19×10^{34}	4.03×10^{34}	5.61×10^{34}	1.27×10^{35}	3.47×10^{34}

Notes.
[a] All quoted error bounds are 90% confidence intervals and the best model is marked in bold.
[b] The abundance for oxygen was frozen to 1.7 and 1 [numbers in brackets] for all fits. Since the errors are similar for both cases, only one set of errors are given.
[c] Emission measure, defined as $\int n_e n_{\rm H}\, dV$: here, d is the distance to CTB 1 (in cm) and n_e and $n_{\rm H}$ are the electron and H densities (in cm^{-3}).
[d] The units for the thermal component $kT_{\rm hard}$ are keV.
[e] Normalization for the power-law component in units of photons keV^{-1} cm^{-2} s^{-1} at 1 keV.
[f] For the energy range 0.6–10.0 keV. The units for the flux are erg cm^{-2} s^{-1} and the units for the luminosity are erg s^{-1}. The luminosity estimates are for an assumed distance of 3.1 kpc.
[g,i] The degree of freedom for southwestern spectra (^{g}) is ∼1039 with both GIS and SIS data, for northeastern spectra^i is 394 with only GIS data.
[h] The numbers in brackets correspond to values derived with the fits with fixed solar abundances.

allowing the neon and iron abundances to vary. Because models with a single thermal component were not sufficient to describe the X-ray spectra, we used a combination of the thermal models VAPEC and VNEI along with a power-law model to jointly fit the *ASCA* spectra: the results of these spectral analyses are given in Table 4. From these fits, we estimate a column density $N_{\rm H} \sim (0.5–0.7) \times 10^{22}$ cm^{-2} and a temperature $kT_{\rm soft} \sim 0.2–0.3$ keV for the soft emission. The soft thermal component has most likely attained thermal equilibrium because fits to this soft emission using the VNEI model resulted in a long ionization timescale ($\tau \sim 1$ (>0.2) $\times 10^{11}$ cm^{-3} s). The hydrogen column density $N_{\rm H}$ and the temperature of the soft component $kT_{\rm soft}$ are in agreement with the analysis of *ROSAT* spectra (Rho 1995; Craig et al. 1997). The inclusion of a second component was necessary for obtaining statistically acceptable fits to the *ASCA* spectra of the southwestern region (with values for χ^2_ν of ∼ 1.1): the addition of a power law with a photon index $\Gamma \sim 2–3$ or a second thermal component with a temperature $kT \sim 3$ keV yields fits with a comparable quality. Unfortunately, due to a low number of counts in the spectra at the higher X-ray energies, we cannot distinguish between different models for the high-energy emission. In Figure 14, we present the GIS and SIS X-ray spectra of the southwest region, fit with the combination of a thermal (VAPEC) and non-thermal (power-law) model. Our results differ from Lazendic & Slane (2006) who fit the extracted *ASCA* spectra from this region with two thermal components in CIE: the softer temperature component featured a temperature $kT = 0.19^{+0.09}_{-0.03}$ keV and a magnesium abundance fixed at solar while the harder temperature component featured a temperature $kT = 0.82^{+0.09}_{-0.06}$ keV and an elevated magnesium abundance (Mg $= 2.7^{+0.9}_{-0.5}$).

Finally, we examine the *ASCA* spectra of the northeast region of CTB 1 which corresponds to the known "breakout" site seen in optical and radio images of this SNR. Like the southwest region, a second component is needed (in addition to a soft thermal component) to derive a statistically acceptable fit. A fit to these spectra using a power-law component for the hard emission is presented in Table 4 and the GIS spectra are presented in Figure 15. For the thermal component, we have first assumed the abundances of oxygen, neon, and iron to be 1.7, 1.6, and 0.4, respectively, equal to the abundances in the "diffuse" region. Second, we assumed solar abundances for the hard component. Although the GIS spectra of the northeastern region feature a stronger Fe L-shell line complex when compared with the spectra of the southwestern region, our spectral fits could not confirm non-solar abundances and the abundances are consistent with solar values.

The photon index derived from fits to the northeast is flatter than the photon index derived from fits for the southwest region: $\Gamma = 1.4$ compared to $\Gamma = 2–3$, respectively. However, the photon statistics at higher energies is poor, making it difficult to determine the true nature of this hard emission. Although the northeast region does correspond to the prominent breakout feature, we do not find evidence for any major differences in the X-ray properties between the northeast and southwestern regions of CTB 1. The fact that no significant variations are seen on large scales in the X-ray properties of CTB 1, coupled with the variations seen on small scales as revealed by the *Chandra*

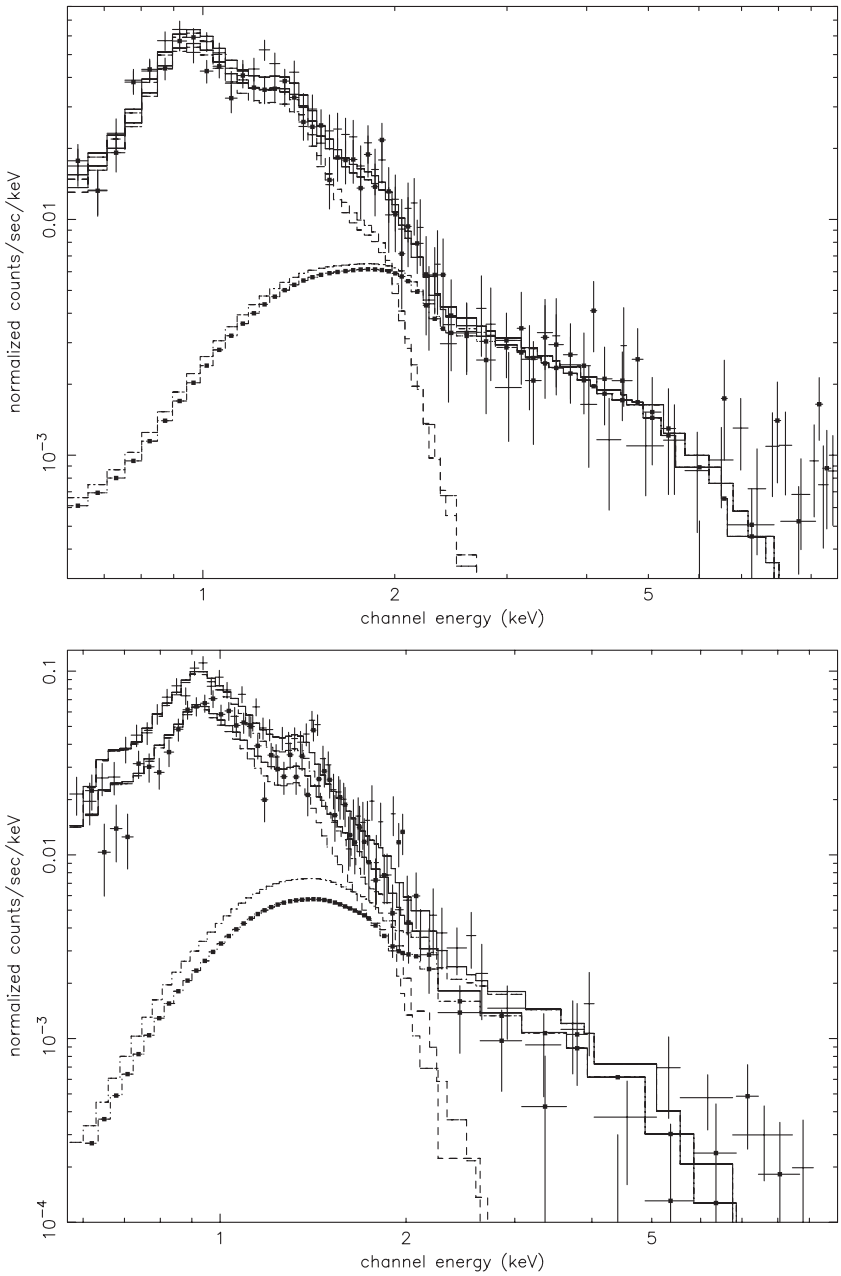

Figure 14. *ASCA* GIS (top) and SIS (bottom) spectra of the southwestern region of CTB 1: the spectra have been fit using the PHABS×(VAPEC+Power Law) model (see Table 4).

observation, indicates that the X-ray emission from this SNR is complex. A parallel may be drawn with the results from *Chandra* observations of 3C 391, another MM SNR: in the case of that source, local spectral differences appeared to be stronger than global ones (Chen et al. 2004). Here, again we find that our results differ from those presented by Lazendic & Slane (2006): for this region, the authors derived an acceptable fit using a single thermal component ($kT = 0.18^{+0.00}_{-0.01}$ keV) in CIE with solar abundances.

4. 1WGA J0001.4+6229—AN X-RAY PULSAR ASSOCIATED WITH CTB 1?

The *ASCA* hard energy image ($E > 1$ keV) revealed a hard source in the northeastern region of CTB 1 which is located just inside the eastern shell of the SNR: the position of this source is R.A. (J2000.0) $00^{h}01^{m}25\overset{s}{.}5$, decl. (J2000.0) $+62^{\circ}29'40''$ with a positional uncertainty of $13''$. This is the discrete X-ray source 1 WGA J0001.4+6229 in the Catalog of *ROSAT* PSPC WGA Sources (White et al. 1994, 1997; Angelini et al. 2000).[12] This X-ray source may possibly be a neutron star associated with CTB 1. We therefore conducted spectral and timing analysis of the X-ray emission from this source using the *ASCA* GIS2 and GIS3 data sets.

The procedure for extracting GIS2 and GIS3 spectra of 1WGA J0001.4+6229 and performing a spectral analysis was the same as for extracting GIS2 and GIS3 spectra of the diffuse emission from HB21 and CTB 1: a circular region 4 arcmin in diameter centered on the source position was used to extract spectra. The total number of counts and the corresponding count rate (over the energy range from 0.6 keV to 10 keV) for our

[12] Also see http://wgacat.gsfc.nasa.gov.

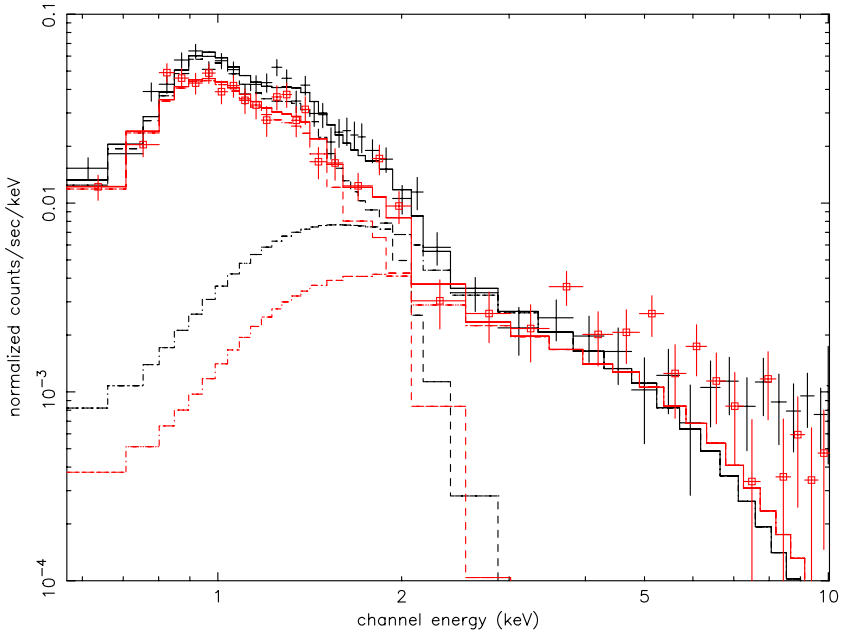

Figure 15. *ASCA* GIS2 spectra of the southwest (in black with crosses) and northeast (in red with squares) regions of CTB 1. Both of these spectra have been fit with a PHABS×(VAPEC+POWER LAW) model. The parameters of the fits to these spectra are listed in Table 4.

(A color version of this figure is available in the online journal.)

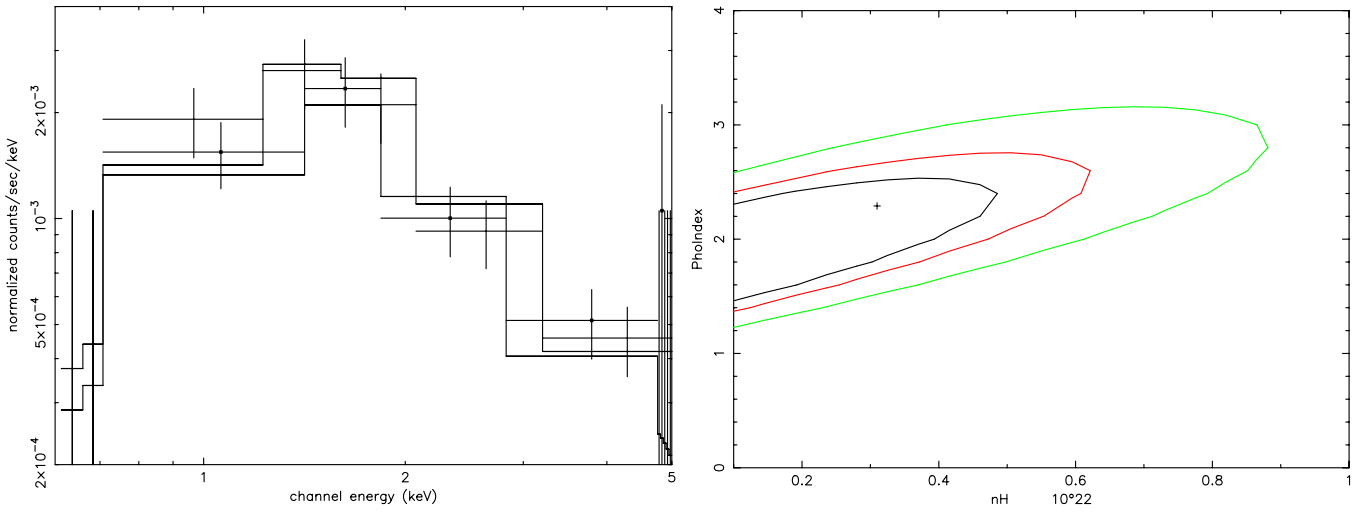

Figure 16. Left: the GIS2/GIS3 spectra of the hard source 1WGA J0001.4 + 6229 as fit with an absorbed power-law model. Right: plot of confidence contours for photon index vs. $N_{\rm H}$ for this fit: a low column density is implied, indicating that the source is Galactic rather than extragalactic. The confidence contours are at the 1σ, 2σ, and 3σ levels. See Section 4.

(A color version of this figure is available in the online journal.)

GIS2 and GIS3 observations were 115 and 103 counts, and $5.71 \pm 0.53 \times 10^{-3}$ and $5.11 \pm 0.51 \times 10^{-3}$ counts per second, respectively. We derived a statistically acceptable joint fit to the spectra using a simple power-law model combined with the same PHABS model mentioned previously for the photoelectric absorption along the line of sight. The parameters of this fit were a column density of $N_{\rm H} = 0.3(< 0.65) \times 10^{22}$ cm^{-2} and a photon index $\Gamma = 2.2^{+0.5}_{-1.2}$: in Figure 16, we present the extracted GIS2/GIS3 spectra together with the best-fit model, and a confidence contour plot for $N_{\rm H}$ and Γ. The derived photon index is typical for rotation-powered pulsars. The column density is consistent with the range of column densities derived in our fits (see Tables 3 and 4) to the CTB 1 spectra, hinting at a possible association. If we fit the extracted spectra for this source with a blackbody model, a temperature of $kT \sim 1.1$ keV is derived (although this fit with $\chi^2_\nu = 0.92$ for 48 degrees of freedom (dof) is inferior to the power-law fit with $\chi^2_\nu = 0.79$). Because of the low derived column density, our estimated absorbed and unabsorbed fluxes for this source are virtually identical: for the GIS2 (GIS3) spectrum, the flux is 5.4×10^{-13} (6.4×10^{-13}) erg cm^{-2} s^{-1}; at the assumed distance to CTB 1, these fluxes correspond to luminosities of 6.2×10^{32} (7.4×10^{32}) erg s^{-1}, respectively. We also performed a timing analysis using the GIS2/GIS3 data sets to search for pulsed X-ray emission from this source and detected a period of 47.6154 ms using the Rayleigh test (a maximum signal of $Z^2 = 31.4$), but the detection is not statistically significant.

We further searched for pulsations from 1WGA J0001.4+6229 with the 100 m Green Bank Telescope (GBT) of the National

Radio Astronomy Observatory (NRAO[13]) on 2004 December 7. The target position was observed for 7.6 hr at a center frequency of 825 MHz. The front end was the GBT Prime Focus 1 receiver to feed the Pulsar Spigot (Kaplan et al. 2005) and Berkeley-Caltech Pulsar Machine (BCPM) back ends. The receiver provided 50 MHz of bandwidth in two orthogonal polarizations that were summed and synthesized into 1024 frequency channels every 81.92 μs in the Spigot and 96 channels of 0.25 MHz width every 144 μs in the BCPM. The interstellar dispersion toward CTB1 is unknown, but we can estimate it with the latest model of Galactic electron density (Cordes & Lazio 2002), which predicts a dispersion measure (DM) of 105 pc cm^{-3} for a distance of 3.1 kpc or DM = 33 pc cm^{-3} at a distance of 1.6 kpc (corresponding to the two distances to CTB 1 that have been published in the literature). We therefore take a conservative upper limit of DM = 1000 to CTB 1 (given the narrow channels and relative long pulsation period the search is not highly DM dependent). The data set was dedispersed with DMs from 0 to 1000 and searched for periodicities using standard folding and fast Fourier-Transform-based techniques. Based on these analyses, we find no significant evidence for pulsations with any period from 1WGA J0001.4+6229.

Assuming that 1WGA J0001.4+6229 is in fact a neutron star associated with CTB 1, a transverse velocity can be estimated. The angular displacement of 1WGA J0001.4+6229 from the center of CTB 1 is 14′ while the radius of the SNR itself is 17′. Therefore, we calculate a transverse velocity $v = 850\ d_{3.1} t_{1.6}^{-1}$ km s^{-1}, where $d_{3.1}$ is the distance to CTB 1 in units of 3.1 kpc and $t_{1.6}$ is the age of the SNR (Fesen et al. 1997) in units of 1.6×10^4 yr. This estimated transverse velocity is high but this may be an overestimate because of the considerable uncertainties associated with estimates of the distance and age of CTB 1: if we assume a distance to the SNR of 1.6 kpc, the transverse velocity is only 420 km s^{-1}. In particular, the published age estimates are based on simple one-dimensional SNR models: the obvious breakout morphology of CTB 1 clearly indicates that such models are not applicable in this case. For comparison, the transverse velocities for neutron stars located off center in their associated SNRs are 375 km s^{-1} in the case of the SNR W44 (Frail et al. 1996) and 250 ± 50 km s^{-1} in the case of the SNR IC 443 (Olbert et al. 2001). It is plausible that 1WGA J0001.4+6229 is associated with CTB 1 but deeper high spatial resolution X-ray observations are needed to examine its spectrum in more detail and search for possible pulsations.

5. PLASMA CONDITIONS IN HB21

We first estimate the density and mass of the X-ray-emitting plasma associated with HB21 based on the emission measures (EMs) derived from our spectral fitting. Our GIS spectral extraction regions extend over approximately 11.′5 × 11.′5 or 5.7 pc × 5.7 pc (2.7 pc × 2.7 pc) at the assumed 1.7 (0.8) kpc distance to HB21. Assuming a cylindrical geometry with the long axis equal to the observed extent of the X-ray plasma (35.′8, corresponding to 17.7 (8.3) pc), the volume of each region is approximately 5.4×10^{58} (5.6×10^{57}) cm^3. From the mean values of our derived EMs (which are approximately the same for all regions and all models), we calculate an electron density $n_e \approx 0.06$ (0.08) cm^{-3} (where we have assumed $n_e \approx 1.2 n_{\rm H}$ and a volume filling fraction of unity based on the smooth appearance and isothermal nature of the X-ray-emitting gas). Based on this value, we estimate the total mass of the X-ray-emitting plasma within the field of view of the *ASCA* observations to be only ≈2.6(1.5) $M_\odot$. When we account for the incomplete spatial coverage of HB21 by the *ASCA* observations, the total X-ray mass could be higher by a factor of 9, which amounts to a total of 23.4 (14) $M_\odot$. The corresponding Si and S masses are $1.7 \times 10^{-3}\ M_\odot$ and $1.3 \times 10^{-3}\ M_\odot$, respectively. The presence of a bright radio shell without associated X-ray emission combined with the detections of an expanding H I shell and infrared emission from shock-cloud interaction regions (Koo & Heiles 1991; Shinn et al. 2009, 2010, and the references therein) imply that HB21 is in a radiative cooling stage. The SNR age inferred from the presence of an expanding ($v_{\rm exp} = 124$ km s^{-1}) H I shell is $t_d = 4.5 \times 10^4$ yr (Koo & Heiles 1991). We can also infer the pressure within HB21 from properties of the X-ray-emitting gas. The total number of particles is $n_{\rm total} = n_e + n_{\rm H} + n_{\rm He} \approx 2 n_e$ for a plasma with cosmic abundances: from our estimated values for electron density and temperature, the corresponding pressure is $P/k = 2 n_e T = 0.9(1.2) \times 10^6$ K cm^{-3}, which as about 2 orders of magnitude higher than the typical ISM pressure. The physical properties of HB21 are summarized in Table 5.

The X-ray properties of HB21 are similar to those measured for many other MM SNRs. First, the presence of an isothermal plasma with a temperature of $kT \sim 0.2$–0.7 keV is consistent with other MM SNRs such as 3C391 (Rho & Petre 1996; Chen et al. 2004), W44 (Rho et al. 1994; Shelton et al. 2004), 3C400.2 (Yoshita et al. 2001), W51C (Koo et al. 2002), W63 (Mavromatakis et al. 2004), and Kes 79 (Sun et al. 2004). This result supports the interpretation that these SNRs are evolved and in the radiative phase as suggested by the presence of

Table 5
Summary of the Physical Properties of HB21 and CTB 1[a]

Property	HB21	CTB 1
Angular size (arcmin)	120 × 90	34
Distance (kpc)	1.7	3.1
Physical diameter (pc)	59 × 45	31
Average radius (pc)	26	15.3
$N_{\rm H}$ (10^{21} cm^{-2})	0.23–0.31	0.57–0.80
kT or Γ	0.63–0.68 keV	0.28 keV, Γ = 2–3 (or 3 keV)
[O/Fe]	...	$4.3^{+10.2}_{-2.5}$
[Ne/Fe]	...	$4.0^{+8.0}_{-2.2}$
n_e (cm^{-3})	0.06	$0.16 f_{\rm soft}^{-1/2}$
M_X[b] ($M_\odot$)	23.4	$40 f_{\rm soft}^{1/2}$
X-ray pressure P/k(K cm^{-3})	0.9×10^6	2.8×10^6
Shock velocity (optical)[c] (km s^{-1})	...	400
Age (optical)[c] (yr)	...	1.6×10^4
Shock velocity (H I shell)[d] (km s^{-1})	124	107?
Age (H I shell)[d] (yr)	4.5×10^4	4.4×10^4
n_0 (H I shell)[d] (cm^{-3})	2.7	...
E_0 (H I shell)[d] (erg)	1.6×10^{51}	...
ΔM (H I shell)[d] ($M_\odot$)	150 ± 10	12 ± 8

Notes.
[a] See Sections 5 and 6.
[b] In the case of HB21, the listed X-ray-emitting mass is for the volume of the whole SNR. The X-ray-emitting mass of just the area of HB21 observed by *ASCA* is 2.6 $M_\odot$.
[c] Fesen et al. (1997).
[d] Koo & Heiles (1991), who assumed distances of 1.1 kpc and 3.2 kpc to HB21 and CTB 1, respectively.

[13] The National Radio Astronomy Observatory is a facility of the National Science Foundation, operated under cooperative agreement by Associated Universities, Inc.

infrared, optical, and H I shells for many of these SNRs. There are no temperature variations and no pronounced enhancements of chemical abundances in HB21 either, just as in many other MM SNRs like 3C 391. These properties of HB21 exemplify the typical X-ray characteristics of MM SNRs as defined by Rho & Petre (1998). At a sufficiently old age ($\sim 10^6$ yr) age, an SNR should exhibit a centrally filled X-ray morphology and eventually merge with the hot ISM gas (Cui & Cox 1992): however, MM SNRs attain this state at a much earlier age ($\sim 10^4$ yr). When a distance of 1.7 kpc to HB21 is assumed, the calculated X-ray-emitting mass of this SNR is comparable to those of other MM SNRs. For standard radiative SNR models, we expect $\sim 100\ M_\odot$ of X-ray-emitting gas at the HB21 age of 4×10^4 yr based on equations given by Cui & Cox (1992) and models presented by Hellsten & Sommer-Larsen (1995). Even more X-ray-emitting gas is expected in conduction models of Cox et al. (1999). This discrepancy between the observed and predicted X-ray-emitting mass is also present in W28 (Rho & Borkowski 2002), but unlike in W28 (where large temperature gradients have been detected), the presence of an isothermal plasma at the center of HB21 suggests that the electron thermal conduction is important (Chevalier 1999). The conduction model of Cox et al. (1999) overpredicts the mass of X-ray-emitting gas: however, this model assumes a uniform ambient ISM while HB21 is known to be interacting with clumpy molecular clouds (Koo et al. 2001; Shinn et al. 2009, 2010). More elaborate X-ray emission models of SNRs in molecular clouds are needed to account for the observed X-ray properties of HB21 and similar MM SNRs.

6. SUPERNOVA EJECTA IN CTB 1

The enhanced abundances of oxygen and neon and low iron abundances in the "diffuse" region (see Table 3) indicate that CTB 1 is likely an oxygen-rich SNR. This SNR was likely produced by a core-collapse SN explosion, because such explosions produce O- and Ne-rich, and Fe-poor ejecta (Nomoto et al. 1997; Woosley & Weaver 1995). This finding is consistent with the presence of a massive star forming environment near CTB 1 (Landecker et al. 1982): in addition, the scenario for the creation of this SNR by a core-collapse SN explosion would be further supported if the discrete X-ray source discussed earlier—1WGA J0001.4+6229—is shown to be a neutron star associated with this SNR. Examples of oxygen-rich SNRs include young sources such as Cas A, N132D, and E0102.2 − 72.3; recently two older SNRs located in the Small Magellanic Cloud (SMC)—SNR B0049-73.6 (Hendrick et al. 2005) and B0103-72.6 (Park et al. 2003)—were also classified as oxygen-rich SNRs. Both of these SMC SNRs show the ejecta material in their interiors surrounded by shells of swept-up ambient material at relatively low X-ray-emitting temperatures. An X-ray-emitting shell might be present in CTB 1, but its detection may be prevented by substantial interstellar absorption in this direction combined with an expected low temperature of the shocked ambient gas.

We estimated the X-ray mass and density of CTB 1 from our fits to the *ASCA* spectra, assuming metal abundances derived from the *Chandra* spectra of the "diffuse" and "soft" regions. The spectral fits to the GIS spectra in the $11\farcm5 \times 11\farcm5$ region imply an electron density of $0.16\, f_{\rm soft}^{-1/2}$ cm^{-3} for the soft thermal component (where $f_{\rm soft}$ is the volume filling factor for this component). The corresponding hydrogen density $n_{\rm H}$ is equal to $n_e/1.2 = 0.13\, f_{\rm soft}^{-1/2}$cm^{-3}; based on this value we estimate the total mass of the X-ray-emitting plasma to be $\approx 40\, f_{\rm soft}^{1/2}\ M_\odot$. From our derived abundances of oxygen, neon, and iron based on *Chandra* data, we estimate the oxygen, neon, and iron masses to be $0.66\, f_{\rm soft}^{1/2}$, $0.11\, f_{\rm soft}^{1/2}$, and $0.03\, f_{\rm soft}^{1/2}\ M_\odot$, respectively. The ratio of [O/Fe] is $4.3^{+10.2}_{-2.5}$ and [Ne/Fe] is $4.0^{+8.0}_{-2.2}$ for CTB 1. The expected ratio of [O/Fe] is 0.75 for a Type Ia explosion and greater than 4 for a core-collapse explosion. These abundances imply that CTB 1 is the remnant of a core-collapse explosion and are consistent with the predictions for a stellar progenitor with a mass of 13–15 $M_\odot$ (Woosley & Weaver 1995; Nomoto et al. 1997), but higher mass stellar progenitors are not excluded.

Finally, we estimate the pressures of the soft and hard components of the X-ray-emitting gas using the parameters of the PHABS×(VAPEC+VAPEC) model: for the soft component, we calculate a corresponding pressure $P/k = 1.1 \times 10^6\ f_{\rm soft}^{-1/2}$ K cm^{-3}. For the hard component (assuming a thermal origin), we first need to calculate the corresponding electron density which we can determine from the electron density of the soft component and the EMs of the soft and hard components (i.e., $n_e({\rm hard}) = n_e({\rm soft})\ [{\rm EM_{hard}/EM_{soft}}]^{1/2}$). From this relation, we obtain $n_e({\rm hard}) = 0.029\ f_{\rm hard}^{-1/2}$ cm^{-3} (here, $f_{\rm hard}$ is the volume filling factor for the hard component) and therefore a corresponding pressure $P/k = 2.0 \times 10^6\, f_{\rm hard}^{-1/2}$ K cm^{-3}. This result implies a factor of four larger filling factor for the hotter gas than the cooler gas if these two components are in pressure equilibrium: a higher filling factor for the hot gas is typical. Assuming $f_{\rm soft} + f_{\rm hard} = 1$, the pressure within CTB 1 is 2.8×10^6 K cm^{-3}. We summarize these inferred physical properties for CTB 1 in Table 5.

CTB 1 therefore belongs to a growing number of known evolved SNRs which feature an enhanced metal abundance in their interiors. An example of another MM SNR which features such enhanced abundances is W44 (Shelton et al. 2004): other similar sources are identified by Lazendic & Slane (2006) (including HB21, which was analyzed both in their study and in the study presented here). In addition, two other Galactic SNRs—the Cygnus Loop (Miyata et al. 1998) and G347.7 + 0.2 (Lazendic et al. 2005)—feature enhanced abundances of metals as well. W49B (Hwang et al. 2000) shows highly enhanced abundances but its age is estimated to be 2000 years (Hwang et al. 2000) and Rho & Petre (1998) describe the source as an atypical MM SNR. Because MM SNRs like CTB 1 are commonly believed to be evolved sources—age estimates of CTB 1 range from 9000 yr (Craig et al. 1997) to 4.4×10^4 yr (Koo & Heiles 1991)—their X-ray spectra are dominated by swept-up material (Rho & Petre 1998). Therefore, the detection of X-ray-emitting material associated with these sources with enhanced metal abundances is unexpected. The detection of O-rich ejecta associated with CTB 1 is particularly noteworthy: CTB 1 may belong to a previously unrecognized class of MM SNRs whose X-ray emission is dominated by O-rich ejecta located within their interiors. As noted previously, another possible member of this particular class of MM SNRs with O-rich ejecta may be HB3 (Lazendic & Slane 2006). We note that O-rich ejecta has been previously detected in the evolved (1.4×10^4 yr old) SMC SNR B0049-73.6 by Hendrick et al. (2005) and it is likely that centrally located ejecta will be found in a number of relatively old Galactic SNRs.

The X-ray-emitting plasma associated with CTB 1 clearly extends through the gap in the crescent-shaped radio shell: Hailey & Craig (1994) and Rho (1995) first noticed this remarkable extension of X-ray emission based on *ROSAT* PSPC

observations. Two scenarios have been proposed to explain the morphology of the observed X-ray emission: Craig et al. (1997) have suggested that the ambient ISM toward the northeastern portion of the SNR was cleared by a supernova (SN) event which took place prior to the birth of CTB 1, and thus a breakout occurred as the SNR expanded into this region of a dramatically lower density. A competing theory for the morphology has been proposed by Yar-Uyaniker et al. (2004), who suggested that the X-ray emission from CTB 1 lies in the interior of a bubble seen in the 21 cm H line, presumably blown by winds of the CTB 1 stellar progenitor. Our X-ray images show that the diffuse X-ray emission in the northeast clearly extends through the relatively narrow break in the optical and radio shell, with the breakout directed into the interior of the bubble seen in the neutral hydrogen line. Such a morphology favors a scenario where an SN explosion occurred within the H I shell, followed by subsequent breakout into the bubble and not an explosion within the bubble itself. Our *ASCA* spectra show little difference between the X-ray properties of the southwest and northeast regions: hints of variations in temperature and abundances exist but better X-ray data are needed to determine whether they are real and not just statistical fluctuations.

7. THE NATURE OF THE HARD X-RAY EMISSION FROM CTB 1

The *ASCA* spectra of the southwestern portion of CTB 1 revealed the presence of a hard component in addition to the soft ($kT \sim 0.28$ keV) component. This hard component may be modeled as a second thermal component with a temperature of $kT \sim 3$ keV or as a power-law continuum with a photon index $\Gamma \sim 2$–3. Hard X-ray emission was also detected by *ASCA* in the northeast region of CTB 1: a power-law component with a photon index $\Gamma\sim 1.4$ (a somewhat lower value compared to the southwest region) combined with a soft thermal component (again with a temperature $kT \sim 0.28$ keV) yields a statistically acceptable fit. The *Chandra* observation of the southwest region of CTB 1 revealed regions of harder emission patches on the scale of an arcminute in size: the spectrum of one of these regions can be modeled by either a single thermal component with an elevated temperature ($kT\sim 0.66$ keV) or as the combination of a soft thermal component ($kT \sim 0.28$ keV) and a power-law component with a photon index $\Gamma \sim 2.0$ (see Tables 3 and 4). The "hard" region observed by *Chandra* is only a few arcminutes from the center of CTB 1 and well inside the radio-emitting shell of the SNR: it is diffuse in nature although the number of counts detected from the source is limited. It is possible that the hard X-ray emission detected by *ASCA* from CTB 1 may be composed of localized hard regions such as this one: unfortunately, we do not have enough counts from this region to distinguish between thermal and non-thermal origins. We note that two other MM SNRs, W28 and IC 443, contain high-temperature thermal plasmas in their interiors (Rho & Borkowski 2002; Kawasaki et al. 2002).

Several possible explanations may be considered for the origin of hard X-ray emission from MM SNRs: first, the hard emission may be caused by temperature variations within the SNR. In the case of CTB 1, this scenario is supported by a good fit to the spectrum of the "hard" region with a thermal component with a much higher than average temperature. SN ejecta may be inhomogeneous in which case a multi-temperature plasma with spatially varying abundances is expected. Alternatively, the "hard" regions may be caused by localized non-thermal emission: such emission has already been detected in IC 443 (Bocchino & Bykov 2003) and γ Cygni (Uchiyama et al. 2002). Additional observations are needed to understand the true nature of the hard X-ray emission from CTB 1.

8. SUMMARY

1. We presented *ASCA* observations of the MM SNR HB21. Our *ASCA* images of this SNR are similar to *ROSAT* images and reveal a diffuse centrally filled X-ray emission located within a radio shell. From X-ray spectra, we measure a column density toward this source and a temperature for the X-ray-emitting plasma of $N_{\rm H} \sim 0.3 \times 10^{22}$ cm^{-2} and $kT \sim 0.7$ keV, respectively: no significant spatial differences in temperature are found. Silicon and sulfur abundances are slightly enhanced relative to solar, particularly for the northwestern region, and no hard component to the X-ray emission was detected. The properties of HB21 are similar to those seen in several other MM SNRs, such as the presence of isothermal plasma. This result supports the interpretation that MM SNRs are evolved sources currently in the radiative phase of evolution: the X-ray properties of HB21 exemplify the primary characteristics of MM SNRs as defined by Rho & Petre (1998).
2. We presented *ASCA* and *Chandra* observations of the MM SNR CTB 1. *ASCA* observations reveal center-filled X-ray emission located within the radio shell: the X-ray emission extends outside the circular shell through the breakout gap in the northeast. While the global X-ray and radio morphology is similar to HB21, the X-ray spectra of CTB 1 and HB21 are very different. The X-ray spectrum of CTB 1 shows several prominent lines such as O Lyα (0.65 keV) and Ne IX (0.9 keV). We find that CTB 1 is likely an oxygen-rich SNR with enhanced abundances of oxygen and neon: this is surprising for an evolved SNR such as CTB 1. The derived abundances are consistent with an explosion of a stellar progenitor with a mass of 13–15 $M_\odot$ and possibly even higher.
3. The *ASCA* spectra of the southwest region of CTB 1 cannot be fit with a single thermal component and instead require the presence of an additional component to account for an excess emission seen at higher energies. Based on *ASCA* and *Chandra* spectra of CTB 1, we derive a column density $N_{\rm H} \sim 0.6 \times 10^{22}$ cm^{-2} and a temperature for the soft emission of $kT_{\rm soft} \sim 0.28$ keV; the hard emission may be modeled either by a thermal component with a temperature $kT_{\rm hard} \sim 3$ keV or by a power-law component with a photon index of $\Gamma \sim 2$–3. Likewise, the *ASCA* spectra of the northeast region of CTB 1 also show an excess at higher energies: these spectra are best fit by a power law with a photon index $\Gamma = 1.4$ plus the soft thermal component. The *Chandra* observation of the southwestern region reveals localized regions of hard emission: one such region is $\sim 1'$ in size. The X-ray spectrum of this region may be fit with either a higher temperature thermal component ($kT = 0.66$ keV) or with the combination of a softer thermal component ($kT = 0.28$ keV) and a power-law component ($\Gamma \sim 2.0$). Because of the poor photon statistics, its true nature is unclear. Possible scenarios for its origin include temperature variations within the X-ray-emitting plasma of CTB 1, including the ejecta, or localized non-thermal X-ray emission.
4. The *ASCA* hard ($E > 1$ keV) image of CTB 1 reveals a point-like source seen in projection against the diffuse emission of CTB 1. This source—denoted as 1WGA

J0001.4+6229 and located at R.A. (J2000.0) $00^h01^m25^s.5$, decl. (J2000.0) $+62^\circ29'40''$—may be a neutron star associated with CTB 1. The GIS2/GIS3 spectra of this source are well fit by a power-law continuum with a photon index $\Gamma = 2.2^{+0.5}_{-1.2}$ (typical for rotation-powered pulsars) and the measured column density is comparable to the column density measured for CTB 1. There is marginal evidence for pulsations in X-ray data at 47.6 ms, but no pulsations have been detected at radio wavelengths.

We thank the referee for many useful comments which helped improve the overall quality of the manuscript. We acknowledge useful discussions with Steven Reynolds regarding the nature of the hard X-ray emission seen toward CTB 1. T.G.P. thanks Ken Ebisawa and Koji Mukai for their assistance with analyzing the *ASCA* data, Keith Arnaud for suggestions during the spectral fitting process and Ilana Harrus for her assistance with making the mosaicked X-ray images of HB21 and CTB 1. T.G.P. also thanks Daniel Harris, Samantha Stevenson, and Nicholas Lee for helpful suggestions regarding the reduction of the *Chandra* observations of CTB 1. We also thank Robert Fesen for kindly sharing his optical images of CTB 1 with us, Bryan Jacoby for assistance with the GBT observations, and Eric Gotthelf for his contributions in searching for pulsed X-ray emission from 1WGA J00001.4+6229. This research has made use of NASA's Astrophysics Data System and data obtained through the High Energy Astrophysics Science Archive Research Center Online Service, provided by the NASA/Goddard Space Flight Center. The research presented in this paper has used data from the Canadian Galactic Plane Survey, a Canadian project with international partners, supported by the Natural Sciences and Engineering Resources Council.

REFERENCES

Angelini, L., Park, S., White, N. E., & Giommi, P. 2000, BAAS, 32, 760
Angerhofer, P. E., Becker, R. H., & Kundu, M. R. 1977, A&A, 55, 11
Arnaud, K. A. 1996, in ASP Conf. Ser. 101, Astronomical Data Analysis Software and Systems V., ed. G. Jacoby & J. Barnes (San Francisco, CA: ASP), 17
Biggs, J. D., & Lyne, A. G. 1996, MNRAS, 282, 691
Bocchino, F., & Bykov, A. M. 2003, A&A, 400, 203
Borkowski, K. J., Lyerly, W. J., & Reynolds, S. P. 2001, ApJ, 548, 820
Brown, R. H., & Hazard, C. 1953, MNRAS, 113, 109
Byun, D.-Y., Koo, B.-C., Tatematsu, K., & Sunada, K. 2006, ApJ, 637, 283
Chen, Y., Su, Y., Slane, P. O., & Wang, Q. D. 2004, ApJ, 616, 885
Chevalier, R. A. 1999, ApJ, 511, 798
Cordes, J. M., & Lazio, T. J. W. 2002, arXiv:0207.156
Cowie, L. L., & McKee, C. F. 1977, ApJ, 211, 135
Cox, D. P., Shelton, R. L., Maciejewski, W., Smith, R. K., Plewa, T., Pawl, A., & Różyczka, M. 1999, ApJ, 524, 179
Craig, W. W., Hailey, C. J., & Pisarski, R. L. 1997, ApJ, 488, 307
Cui, W., & Cox, D. P. 1992, ApJ, 401, 206
Fesen, R. A., Winkler, P. F., Rathore, Y., Downes, R. A., Wallace, D., & Tweedy, R. W. 1997, AJ, 113, 767
Frail, D. A., Giacani, E. B., Goss, W. M., & Dubner, G. 1996, ApJ, 464, L165
Freeman, P. E., Kashyap, V., Rosner, R., & Lamb, D. Q. 2002, ApJS, 138, 185
Green, D. A. 2009a, Bull. Astron. Soc. India, 37, 45
Green, D. A. 2009b, A Catalogue of Supernova Remnants (2009 March Version), Astrophysics Group, Cavendish Laboratory, Cambridge, UK, http://www.mrao.cam.ac.uk/surveys/snrs/
Hailey, C. J., & Craig, W. W. 1994, ApJ, 434, 635
Hailey, C. J., & Craig, W. W. 1995, ApJ, 455, L151
Hamilton, A. J. S., Sarazin, C. L., & Chevalier, R. A. 1983, ApJS, 51, 115
Hellsten, U., & Sommer-Larsen, J. 1995, ApJ, 453, 264
Hendrick, S. P., Reynolds, S. P., & Borkowski, K. J. 2005, ApJ, 622, L117
Humphreys, R. M. 1978, ApJS, 38, 309
Hwang, U., Petre, R., & Hughes, J. P. 2000, ApJ, 532, 970
Kaplan, D. L., et al. 2005, PASP, 117, 643
Kawasaki, M. T., Ozaki, M., Nagase, F., Masai, K., Ishida, M., & Petre, R. 2002, ApJ, 572, 897
Koo, B.-C., & Heiles, C. 1991, ApJ, 382, 204
Koo, B.-C., Lee, J.-J., & Seward, F. D. 2002, AJ, 123, 1629
Koo, B.-C., Rho, J., Reach, W. T., Jung, J., & Mangum, J. G. 2001, ApJ, 552, 175
Kothes, R., Fedotov, K., Foster, T. J., & Uyaniker, B. 2006, A&A, 457, 1081
Kundu, M. R. 1971, ApJ, 165, L55
Kundu, M. R., Becker, R. H., & Velusamy, T. 1973, AJ, 78, 170
Landecker, T. L., Roger, R. S., & Dewdney, P. E. 1982, AJ, 87, 1379
Lazendic, J. S., & Slane, P. O. 2006, ApJ, 647, 350
Lazendic, J., Slane, P. O., Hughes, J. P., Chen, Y., & Dame, T. M. 2005, ApJ, 618, 733
Leahy, D. A. 1987, MNRAS, 228, 907
Leahy, D. A. 2006, ApJ, 647, 1125
Leahy, D. A., & Aschenbach, B. 1996, A&A, 315, 260
Liedahl, D. A., Osterheld, A. L., & Goldstein, W. H. 1995, ApJ, 438, L115
Lorimer, D. R., Lyne, A. G., & Camilo, F. 1998, A&A, 331, 1002
Mavromatakis, F., Aschenbach, B., Boumis, P., & Papamastorakis, J. 2004, A&A, 415, 1051
Mavromatakis, F., Xilouris, E. M., & Boumis, P. 2007, A&A, 461, 991
Miyata, E., Tsunemi, H., Kohmura, T., Suzuki, S., & Kumagai, S. 1998, PASJ, 50, 257
Nomoto, K., Hashimoto, M., Tsujimoto, T., Thielemann, F.-K., Kishimoto, N., Kubo, Y., & Nakasato, N. 1997, Nucl. Phys., 616, 79
Olbert, C. M., Clearfield, C. R., William, N. E., Keohane, J. W., & Frail, D. 2001, ApJ, 554, L205
Pannuti, T. G., & Rho, J. 2004, BAAS, 36, 1521
Park, S., Hughes, J. P., Burrows, D. N., Slane, P. O., Nousek, J. A., & Garmire, G. P. 2003, ApJ, 598, L95
Reach, W. T., Rho, J., & Jarrett, T. H. 2005, ApJ, 618, 297
Rho, J. 1995, PhD thesis, Univ. Maryland
Rho, J., & Borkowski, K. J. 2002, ApJ, 575, 201
Rho, J., & Petre, R. 1996, ApJ, 467, 698
Rho, J., & Petre, R. 1998, ApJ, 503, L167
Rho, J., Petre, R., Schlegel, E. M., & Hester, J. 1994, ApJ, 430, 757
Saken, J. M., Fesen, R. A., & Shull, J. M. 1992, ApJS, 81, 715
Shelton, R. L., Cox, D. P., Maciejewski, W., Smith, R. K., Plewa, T., Pawl, A., & Różyczka, M. 1999, ApJ, 524, 192
Shelton, R. L., Kuntz, K. D., & Petre, R. 2004, ApJ, 611, 906
Shinn, J.-H., Koo, B.-C., Burton, M. G., Lee, H.-G., & Moon, D.-S. 2009, ApJ, 693, 1883
Shinn, J.-H., Koo, B.-C., Burton, M., Lee, H.-G., & Moon, D.-S. 2010, Adv. Space Res., 45, 445
Slane, P., Smith, R. K., Hughes, J. P., & Petre, R. 2002, ApJ, 564, 284
Smith, R. K., & Brickhouse, N. S. 2000, RevMexAA Conf. Ser., 9, 134
Smith, R. K., Brickhouse, N. S., Liedahl, D. A., & Raymond, J. C. 2001a, in ASP Conf. Ser. 247, Spectroscopic Challenges of Photoionized Plasmas, ed. G. Ferland & D. W. Savin (San Francisco, CA: ASP), 161
Smith, R. K., Brickhouse, N. S., Liedahl, D. A., & Raymond, J. C. 2001b, ApJ, 556, L91
Smith, R. K., & Hughes, J. P. 2010, ApJ, 718, 583
Snowden, S. L., McCammon, D., Burrows, D. N., & Mendenhall, J. A. 1994, ApJ, 424, 714
Sun, M., Seward, F. D., Smith, R. K., & Slane, P. O. 2004, ApJ, 605, 742
Tanaka, Y., Inoue, H., & Holt, S. S. 1994, PASJ, 46, L37
Tatematsu, K., Fukui, Y., Landecker, T. L., & Roger, R. S. 1990, A&A, 237, 189
Taylor, A. R., et al. 2003, AJ, 125, 3145
Tian, W.-W., & Leahy, D. 2006, Chin. Astron. Astrophys., 6, 543
Uchiyama, Y., Takahashi, T., Aharonian, F. A., & Mattox, J. R. 2002, ApJ, 571, 866
Velusamy, T., & Kundu, M. R. 1974, A&A, 32, 375
Weisskopf, M. C., Brinkman, B., Canizares, C., Garmire, G., Murray, S., & van Speybroeck, L. P. 2002, PASP, 114, 1
White, N. E., Angelini, L., & Giommi, P. 1997, in All-Sky X-ray Observatories in the Next Decade, ed. M. Matsuoka & N. Kawai (Japan: RIKEN), 41
White, N. E., Giommi, P., & Angelini, L. 1994, IAU Circ., 6100, 1
White, R. L., & Long, K. S. 1991, ApJ, 373, 543
Wilson, R. W., & Bolton, J. G. 1960, PASP, 72, 331
Woosley, S. E., & Weaver, T. A. 1995, ApJS, 101, 181
Yar-Uyaniker, A., Uyaniker, B., & Kothes, R. 2004, ApJ, 616, 247
Yoshita, K., Tsunemi, H., Miyata, E., & Mori, K. 2001, PASJ, 53, 93